Journal of Drug Delivery Science and Technology 123 (2026) 108416

Contents lists available at ScienceDirect

Journal of Drug Delivery Science and Technology

journal homepage: www.elsevier.com/locate/jddst

Therapeutic effects of mannose modified ciprofloxacin and matrine liposome on intracellular bacterial infections from "superficial to deep"

Fangjin Lu [a,b], Ping Mu [c,d,e], Lin Zhu [c,d,e], SiTong Wang [e], Zhong Zhang [e,*,1], Jiao Wang [c,d,e,**,1]

[a] Department of Pharmaceutical Analysis, School of Pharmaceutical Sciences, Shenyang Medical College, Shenyang, 113004, China
[b] Shenyang Key Laboratory for Screening Biomarkers of Tumor Progression and Targeted Therapy of Tumors, Shenyang Medical College, Shenyang, 113004, China
[c] Key Laboratory of Human Ethnic Specificity and Phenomics of Critical Illness in Liaoning Province, Shenyang Medical College, Shenyang, 113004, China
[d] Shenyang Key Laboratory for Phenomics, Shenyang Medical College, Shenyang, 113004, China
[e] School of Basic Medicine, Shenyang Medical College, Shenyang, Liaoning, 113004, China

ARTICLE INFO

Keywords:
Intracellular bacteria
Antibiotics
Targeted liposomes
Matrine
Infections of different depths

ABSTRACT

Introduction: Intracellular bacterial infections remain a major challenge in clinical antibiotic therapy. Surface-modified nanoliposomes may improve targeted, sustained, and precise drug delivery. In this study, we developed a mannose-modified liposomal co-delivery system containing ciprofloxacin (Cip) and matrine (MT) (Man-Cip&MT-lips) to improve the treatment of intracellular bacterial infections at different tissue depths.

Methods: Liposomes were prepared using the thin-film dispersion method combined with the ammonium sulfate gradient method, followed by physicochemical characterization. The targeting ability, antibacterial activity, therapeutic efficacy against intracellular bacterial infections at different depths in vitro and in vivo, and biosafety of the liposomes were evaluated.

Results: Man-Cip&MT-lips exhibited a spherical morphology with a smooth surface and uniform distribution. The formulation showed enhanced uptake by infected RAW264.7 macrophages and favorable antibacterial activity, including biofilm inhibition and clearance. In addition, Man-Cip&MT-lips demonstrated improved therapeutic effects in in vitro and in vivo models of bacterial infections ranging from superficial to deep tissues.

Conclusion: Both in vitro and in vivo results suggest that Man-Cip&MT-lips may enhance macrophage-targeted delivery and improve the treatment of intracellular bacterial infections. This liposomal co-delivery strategy shows potential as a therapeutic approach for bacterial infections at different tissue depths.

1. Introduction

Bacterial infections present a significant challenge to global public health, as they can invade the human body through various routes and cause a range of diseases [1], including wound infections, pneumonia, and gastrointestinal infections [2–4]. This situation poses a severe threat to human health and safety. Since the advent of antibiotics such as penicillin and polymyxin, humanity has made remarkable strides in combating bacterial infections [5,6]. However, intracellular infections caused by bacteria remain a critical issue in clinical antibiotic therapy [7,8]. It has been reported that a substantial number of chronic recurrent diseases are primarily attributed to intracellular pathogenic bacterial infections [9]. Pathogenic bacteria residing within host cells can evade the host immune system by mimicking host enzymes or secreting specific proteins through virulence factors, which provide a degree of protection for the intracellular bacteria [10,11]. These mechanisms contribute to prolonged intracellular bacterial infections, rendering them difficult to eradicate.

Currently, antibiotics continue to be used clinically for the treatment of intracellular bacterial infections. Ciprofloxacin (Cip) is a quinolone antibiotic that exerts its bactericidal effect by inhibiting bacterial DNA gyrase and topoisomerase IV, thereby interfering with the replication,

* Corresponding author.
** Corresponding author. Key laboratory of Human Ethnic Specificity and Phenomics of Critical Illness in Liaoning Province, Shenyang Key Laboratory for Phenomics, School of Basic Medicine, Shenyang Medical College, Shenyang, Liaoning, 113004, China.
E-mail addresses: zhangzhong369@symc.edu.cn (Z. Zhang), 1336537579@qq.com (J. Wang).
[1] These authors contributed equally to this work.

https://doi.org/10.1016/j.jddst.2026.108416
Received 22 July 2025; Received in revised form 28 April 2026; Accepted 1 May 2026
Available online 11 May 2026
1773-2247/© 2026 Elsevier B.V. All rights are reserved, including those for text and data mining, AI training, and similar technologies.

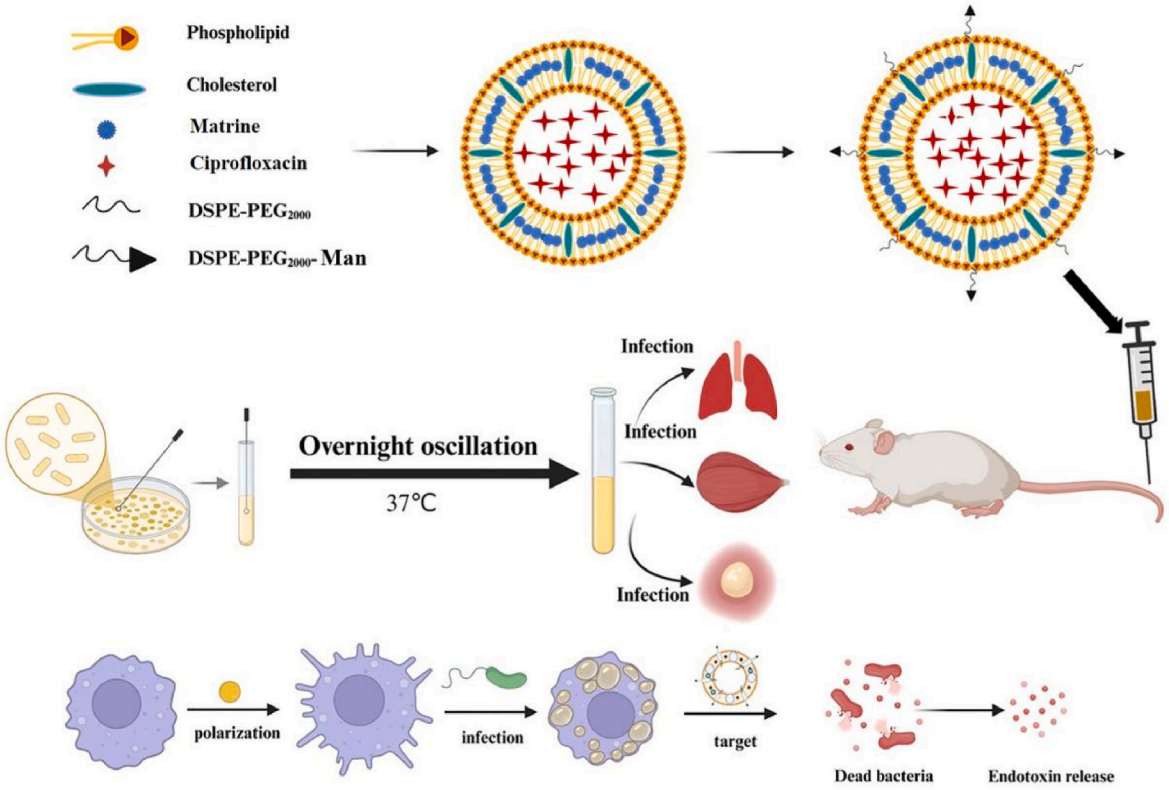


Fig. 1. The strategy diagram of mannose-modified liposomes co-delivering Ciprofloxacin and Matrine to effectively inhibit intracellular bacterial infection in macrophages.

transcription, and repair of bacterial DNA [12–14]. Cip exhibits potent antibacterial activity against most Gram-negative bacteria and also demonstrates antibacterial effects against certain Gram-positive bacteria. However, its use is frequently associated with severe gastrointestinal and central nervous system reactions [15], and it exhibits some cross-resistance with other antibiotics [16]. Matrine (MT) is an alkaloid extracted from the leguminous plant *Sophora flavescens* Aiton, which disrupts bacterial cell membranes and cell walls, inhibits biofilm formation, and interferes with bacterial metabolism, thereby suppressing bacterial growth [17,18]. However, the in vivo activity of matrine is limited, its duration of action is short, and adverse reactions often accompany its use, which restricts the full realization of its clinical efficacy [19].

Over two-thirds of the antibiotics employed against intracellular bacterial infections—including ciprofloxacin—display limited therapeutic efficacy because they cannot readily penetrate host-cell membranes to access the intracellular milieu where pathogens reside. [20]. Even for those antibiotics that can traverse host cells, the intracellular concentration remains insufficient to eliminate bacteria effectively, owing to cellular metabolism and robust drug efflux systems. Nanomaterials, with their unique physicochemical properties, present new strategies for the treatment of bacterial infections [21,22].

For a long time, the targeted delivery of therapeutic compounds to infected sites has posed a significant challenge in the treatment of bacterial infections. Nanoliposomes, when surface-modified with ligands, can achieve targeted, sustained, and precise drug delivery, thereby increasing the concentration of drugs at the infection site [23]. Mannose receptors, primarily expressed on the surfaces of immune cells such as macrophages, mediate the recognition, uptake, and phagocytosis of pathogens by these cells. When mannose-modified drug carriers encounter macrophages, the mannose groups specifically bind to the receptors, enabling the drug carriers to accurately recognize and attach to the surface of macrophages. This interaction facilitates the internalization of the mannose-modified drug carriers, along with their cargo, into the cells [24,25].

Based on this background, we constructed a mannose-modified liposomal co-delivery system containing Cip and MT (see Fig. 1). According to the preparation method and the physicochemical properties of the two drugs, MT was presumed to be mainly distributed in the aqueous core, while Cip was inferred to be associated with the phospholipid bilayer. This liposomal system may provide a promising strategy for improving the treatment of intracellular bacterial infections.

2. Methods

2.1. Materials and reagents

Polyethylene glycol-distearoyl-sn-glycero-3-phosphoethanolamine ($DSPE\text{-}PEG_{2000}$) was obtained from NOF Corporation, Tokyo, Japan. The $DSPE\text{-}PEG_{2000}$-Man was synthesized and provided by Xi'an Ruixi Biological Technology Co., Ltd., Xi'an, China. Soluplus was sourced from BASF, Germany. $TPGS_{1000}$, Cip, MT, Sephadex G-50, coumarin 6 (Cou), 3,3,3,3-tetramethylindotricarbocyanine iodide (DiR), Hoechst 33342, and LB medium were acquired from Dalian Meilun Biotechnology Co., Ltd., Dalian, China. The Live/Dead Bacterial Staining Kit, Sirius Red Staining Kit, and ELISA Detection Kit were procured from Solarbio Science and Technology Co., Ltd., Beijing, China. The HE staining Kit and Masson Staining Kit were obtained from Obiory Technology Co., Ltd., Shenyang, China. The MMP and NF-κB-p65 antibody were sourced from Bioss Biotechnology Co., Ltd., Beijing, China. Methicillin-resistant *Staphylococcus aureus* (MRSA, ATCC29213) and *Pseudomonas aeruginosa* (*P. aeruginosa*, ATCC27853) were acquired from Zhongke Quality Testing Biotechnology Co., Ltd., Beijing, China.

Table 1
Formulations of different preparations.

	DSPE-PEG$_{2000}$- Man	DSPE-PEG$_{2000}$	EPC	Chol	Cip	MT	Cou	RhoB	DiR
Control-lips	-	+	+	+	-	-	-	-	-
Cip&MT-lips	-	+	+	+	+	+	-	-	-
Man-Cip&MT-lips	+	+	+	+	+	+	-	-	-
Cou-lips	-	+	+	+	-	-	+	-	-
Man-Cou-lips	+	+	+	+	-	-	+	-	-
RhoB-lips	-	+	+	+	-	-	-	+	-
Man-RhoB-lips	+	+	+	+	-	-	-	+	-
DiR-lips	-	+	+	+	-	-	-	-	+
Man-DiR-lips	+	+	+	+	-	-	-	-	+

Note: "+" indicates that the preparation contains a drug, and "-" indicates that the preparation does not contain a drug.

2.2. Preparation of liposomes

In this study, liposomes were prepared using the thin-film dispersion method in conjunction with the ammonium sulfate gradient method [26]. Accurately weigh the prescribed amounts of DSPE-PEG$_{2000}$-Man, DSPE-PEG$_{2000}$, EPC, Chol, and Cip (molar ratio 1:1.07:58.4:37.9:4.42), dissolve them in methanol and rotary-evaporated to a thin film. The film was hydrated with $(NH_4)_2SO_4$ (250 mM), sonicated on ice for 10 min (500 W, 10 s on/5 s off, JY92-IIDN, Ningbo Scientz). The hydrated liquid was dialysed in the dark for 24 h using 12–14 kDa MWCO bags. MT was separately film-formed from methanol and hydrated with the dialysed liposomes at 40 °C for 10 min. Free MT was removed on a Sephadex G-50 column to afford Man-Cip&MT-lips. During the lipid film formation stage, Cip and MT were not added, and PBS was used instead of ammonium sulfate solution for hydration to obtain Cou-lips, Man--Cou-lips, DiR-lips, and Man-DiR-lips (see Table 1). Blank liposomes without drugs (Control-lips) were prepared following the above method and subjected to dialysis. Subsequently, RhoB was co-incubated with the dialyzed Control-lips to obtain RhoB-lips and Man-RhoB-lips.

2.3. Characterization of liposomes

After successfully preparing the liposomes, Control-lips, Cip-lips, MT-lips, Cip&MT-lips, and Man-Cip&MT-lips were placed in vials. A laser pen was employed to shine through one side of the vials to determine whether the laser passed through to the other side, thereby confirming whether liposomes exist in the solution. The particle size, zeta potential, and polydispersity index (PDI) of Cip&MT-lips and Man-Cip&MT-lips were measured using the Litesizer 500 laser nanoparticle size analyzer. The absorption spectra of free Cip, free MT, Control-lips, Cip&MT-lips, and Man-Cip&MT-lips were obtained using a FTIR spectrometer (Nicolet iS50, Thermo Scientific). Add small amounts of the prepared freeze-dried powders of free Cip, free MT, Control-lips, Cip&MT-lips, and Man-Cip&MT-lips into appropriate amount of potassium bromide, grind thoroughly, and press into tablets for infrared spectroscopy analysis. The morphology of Cip&MT-lips and Man-Cip&MT-lips was examined using a Tecnai G220 transmission electron microscope.

The encapsulation efficiency (EE) of the two drugs in the liposomes was measured separately using a high-performance liquid chromatography (HPLC, Agress1100, Dalian Elite Analytical Instruments Co., Ltd.) instrument. Take 1 mL of Man-Cip&MT-lips and pass it through a Sephadex G-50 column, eluting with PBS to separate unencapsulated free drugs. Collect the eluted liposome fraction, add methanol for demulsification, vortex, and centrifuge at 12,000 rpm for 3 min. Take the supernatant for HPLC analysis to determine the total amount of drugs encapsulated in the liposomes (Wpost). Separately, take an unseparated sample from the same batch of liposomes, perform demulsification and measurement using the same method to obtain the total drug amount (Wpre). The EE was calculated using the formula: $W_{post}/W_{pre} \times 100\%$, where W_{post} represents the drug content in the liposomes after column passage, and W_{pre} indicates the drug content in the liposomes before column passage.

2.4. Evaluation of in vitro targeting of liposomes

To investigate the active targeting of liposomes, we assessed their targeting capabilities towards RAW264.7 cells infected with bacteria and towards the bacteria themselves. RAW264.7 cells in the logarithmic growth phase were seeded at a density of 2×10^5 cells per well in a six-well plate and incubated overnight at 37 °C. When the cells reached 70% confluence, MRSA or *P. aeruginosa* were inoculated into the wells at a multiplicity of infection (MOI) of 10 and incubated for an additional hour to establish an intracellular bacterial infection model. The wells were washed three times with PBS, and fresh medium was added. Subsequently, free Cou (Cou), Cou-liposomes, and Man-Cou-liposomes were added to the wells, with the final concentration of Cou being 3 μM. After 3 h, the cells in the plate were collected and washed three times with PBS. The fluorescence intensity in RAW264.7 cells infected with MRSA or *P. aeruginosa* was measured using a FACScan flow cytometer (BD Biosciences, NJ, USA) to evaluate the targeting ability of the liposomes.

Co-incubate 1×10^8 CFU/mL of MRSA or *P. aeruginosa* with Cou-labeled liposomes for 0.5, 1, 1.5, and 2 h, ensuring a final Cou concentration of 3 μM. After washing the bacteria three times with PBS, stain them with Hoechst 33342 in the dark for 15 min. Following the staining procedure, observe the targeting of the liposomes using a fluorescence microscope (Nikon Eclipse E800, Nikon, Tokyo) and perform quantitative fluorescence analysis with Image J software.

SYTO-9 was co-incubated with MRSA or *P. aeruginosa* for 2 h to construct green fluorescent-labeled bacteria. RAW264.7 cells in the logarithmic growth phase were seeded in six-well plates at a density of 2×10^5 cells per well. When the cells reached 70% confluence, fluorescent-labeled MRSA or *P. aeruginosa* were inoculated into the wells at a MOI of 10 and further incubated for 1 h. Fresh medium containing 50 μg/mL gentamicin was added to the culture for 0.5 h to eliminate extracellular bacteria. The medium was then replaced with fresh medium, and free RhoB, RhoB-liposomes, and Man-RhoB-liposomes were added for incubation for 4 h. After staining with Hoechst 33342 in the dark for 15 min, the plate was washed three times, and the targeting of liposomes to cells was observed using a fluorescence microscope.

2.5. Determination of minimum inhibitory concentration

The minimal inhibitory concentrations (MICs) of various liposomes against MRSA or *P. aeruginosa* were determined using the broth dilution method. MRSA or *P. aeruginosa* was inoculated onto LB solid medium and incubated at 37 °C for 12 h. Once single colonies appeared on the medium, a colony was selected and transferred into liquid medium, followed by incubation at 37 °C in a shaking incubator for an additional 12 h. The bacteria were washed with PBS, adjusted to a concentration of 1×10^6 CFU/mL, and subsequently inoculated into a 96-well plate. Free CIP (CIP), free CIP and with MT (CIP&MT), CIP&MT-liposomes, and Man-CIP&MT-liposomes were added to the wells of the plate, with CIP concentrations of 20, 10, 5, 2.5, 1.25, 0.625, and 0.3125 μM,

respectively. The incubation continued at 37 °C for 12 h, during which bacterial growth in the wells was observed. The MIC is defined as the minimum concentration of the drug that inhibits bacterial growth. Additionally, Gram staining was employed for the preliminary identification of MRSA or *P. aeruginosa*.

2.6. Dynamic observation of bacterial growth

Dynamically monitor the inhibitory effects of various preparation on bacterial growth. Adjust the concentration of MRSA or *P. aeruginosa* to 1×10^6 CFU/mL and inoculate into a 96-well plate. Add CIP, CIP&MT, CIP&MT-lips, and Man-CIP&MT-lips to the wells individually to achieve a final CIP concentration of 2.5 μM, using PBS as a blank control, and incubate at 37 °C. Measure the OD600 values of the bacteria at 0, 4, 8, 12, 16, 20, and 24 h, and plot the corresponding time-growth curve of the bacteria.

2.7. The zone of inhibition test

The antibacterial effect of liposomes was evaluated using the inhibition zone test. The concentrations of MRSA or *P. aeruginosa* were adjusted to 1×10^6 CFU/mL and inoculated onto LB solid agar plates. Antibiotic sensitivity discs were evenly placed on the LB solid agar plates, and 30 μL of CIP, CIP&MT, CIP&MT-lips, and Man-CIP&MT-lips were slowly dripped onto the discs, respectively, achieving a final concentration of 2.5 μM for CIP. The plates were incubated at 37 °C for 24 h, and the diameters of the inhibition zones surrounding the antibiotic sensitivity discs were measured using a vernier caliper.

2.8. Bacterial live/dead staining

The effects of different liposomes on bacteria were examined using a live/dead bacterial staining kit. The concentrations of MRSA or *P. aeruginosa* were adjusted to 1×10^6 CFU/mL and placed in tubes. CIP, CIP&MT, CIP&MT-lips, and Man-CIP&MT-lips were added to the tubes with the final concentration of CIP set at 2.5 μM. After incubating the bacteria with the drugs for 4 h, the bacteria were washed three times with PBS and subjected to live/dead bacterial staining. The live/dead staining solution was prepared containing 2 μM SYTO-9 and 1 μM PI, and the bacteria were stained in the dark at room temperature for 15 min. Following three washes with PBS, the bacteria were observed using an inverted fluorescence microscope.

2.9. Post-treatment colony count

Spread the bacteria onto the plate to observe the inhibitory effect of the drug on the bacteria more intuitively. The concentrations of MRSA or *P. aeruginosa* were adjusted to 1×10^6 CFU/mL and placed in an tube. CIP, CIP&MT, CIP&MT-lips, and Man-CIP&MT-lips were added to the tube, with the final concentration of CIP being 2.5 μM. After incubating the bacteria with the drugs for 4 h, the bacteria were inoculated onto LB solid plates and further incubated for 24 h. Following this incubation period, the colonies on the solid plates were counted.

2.10. Investigation of biofilm inhibition

The effect of liposomes on bacterial biofilms was investigated using crystal violet staining. The concentrations of MRSA or *Pseudomonas aeruginosa* were adjusted to 1×10^7 CFU/mL and placed in a 48-well plate. Simultaneously, CIP, CIP&MT, CIP&MT-lips, and Man-CIP&MT-lips were added to the wells, with a final concentration of CIP set at 2.5 μM. The plate was incubated at 37 °C to assess the inhibitory effects of liposomes on biofilm formation. After 48 h, the planktonic bacteria were removed, and the biofilms in the wells were stained with crystal violet solution for 15 min. The excess crystal violet dye in the wells was gently washed away with PBS. Following natural drying, the biofilm was dissolved using 33% acetic acid, and the OD was measured at 595 nm.

After adjusting the concentration of MRSA or *P. aeruginosa* to 1×10^7 CFU/mL, inoculate them into a 48-well plate. Place the plate in a 37 °C incubator to cultivate the biofilm. After 48 h, gently replace the medium in the plate and simultaneously add CIP, CIP&MT, CIP&MT-lips, and Man-CIP&MT-lips, ensuring that the final concentration of CIP is set at 5 μM, to investigate the inhibitory effects of different liposomes on mature biofilms. Continue incubation for an additional 24 h, and then employ the same method to perform crystal violet staining on the biofilm. Besides this, resuspend the biofilm in PBS, inoculate the bacteria onto LB solid medium, and incubate at 37 °C for 24 h. Finally, count the colonies on the plate.

2.11. Construction of animal models

We established bacterial infection models of increasing complexity, specifically the "skin-muscle-lung" bacterial infection models. BALB/c female mice were obtained from Liaoning Changsheng Biotechnology Co., Ltd. (Shenyang, China). The mice were housed with free access to food and water, under natural lighting, and maintained at a constant temperature of 23 °C. All animal experiments in this study were performed in compliance with the ARRIVE guidelines and approved by the Animal Ethics Committee of Liaoning University Of Traditional Chinese Medicine (Ethics Approval Number: 210000420230202) for Shenyang Medical College. All procedures were conducted in accordance with the NIH Guide for the Care and Use of Laboratory Animals (NIH Publications No. 8023, revised 1978). ARRIVE Guidelines. The concentration of MRSA in the logarithmic growth phase was adjusted to 1×10^8 CFU/mL 100 μL of MRSA was subcutaneously inoculated into the exposed skin. The appearance of redness, swelling, and suppuration at the inoculation site indicated the successful establishment of the skin bacterial infection model. 100 μL of MRSA was injected into the muscle. The model is considered successfully established when the mouse's muscles exhibit redness and swelling, accompanied by mobility difficulties. The concentration of MRSA in the logarithmic growth phase was adjusted to 1×10^9 CFU/mL and the nasal drip method was employed to construct the MRSA lung infection model, which is deemed successfully constructed when the mouse exhibits coughing accompanied by rapid breathing.

2.12. Evaluation of the in vivo targeting ability of liposomes

The mice were randomly divided into four groups: the control group, the free DiR group, the DiR-lips group, and the Man-DiR-lips group, with saline serving as the control. Following the successful establishment of the model, the fluorescent probe DiR was injected into the tail vein of mice in each group. Mice with skin and muscle infections were anesthetized and placed in a small animal in vivo imaging system (IVScope 8200; QINXIANG, China) to observe the distribution of the fluorescent probe. At 6 and 12 h, one mouse with a lung infection was sacrificed from each group, and the heart, liver, spleen, lung, and kidney were removed and placed in the small animal in vivo imaging system to observe the distribution of the probe.

2.13. In vivo therapeutic efficacy evaluation

Mice were randomly divided into five groups: the model group, the free Cip group (Cip), the free Cip and MT group (Cip&MT), the CIP&MT-lips group, and the Man-CIP&MT-lips group. Administration occurred every other day for a total of three treatments, with a Cip concentration of 0.22 mg/kg in each group's formulation. The status of the infected sites in the skin and muscle of the mice was recorded the day after the last administration. Blood was collected from mice with infections at varying depths, and the mice were subsequently euthanized. The skin, muscle, and lung tissues from the infected sites were embedded and sectioned. Hematoxylin and eosin (HE) staining was performed to

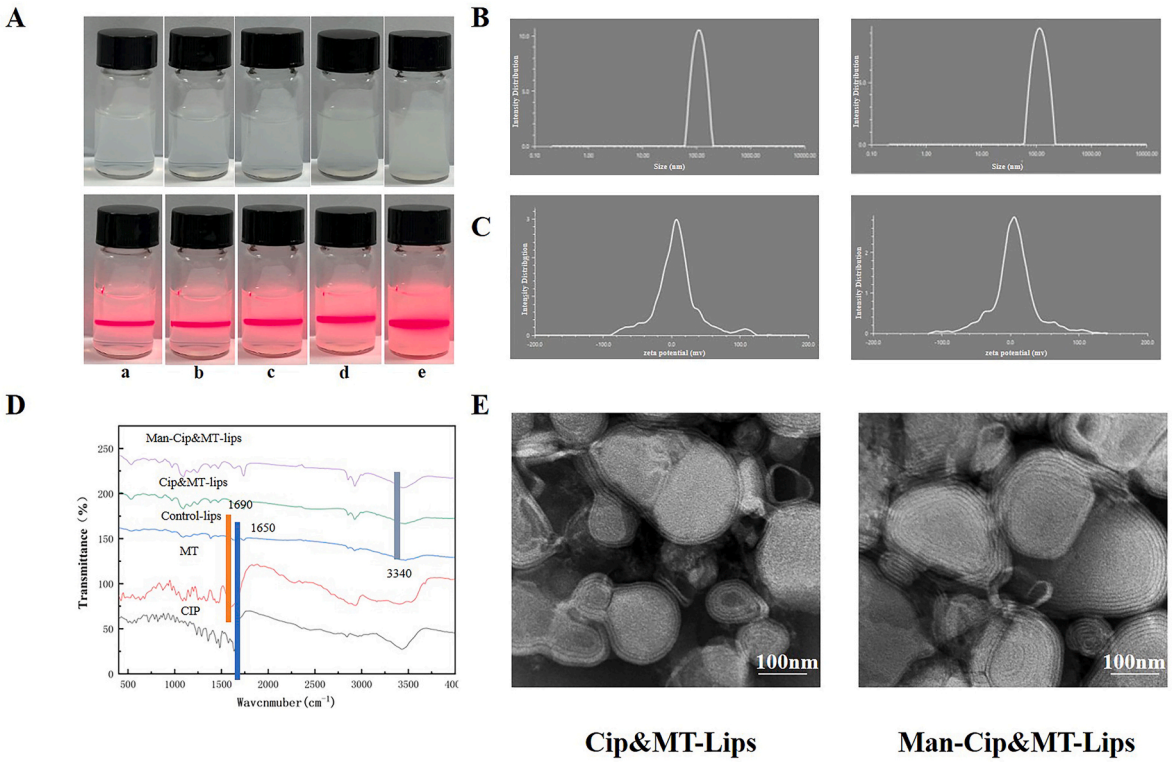


Fig. 2. Preparation and characterization of liposomes. (A) Appearance and transmittance of different liposomes a.Control-lips, b.Cip-lips, c.MT-lips, d.Cip&MT-lips, e. Man-Cip&MT-lips. (B) Particle size distribution of different liposomes. The average particle sizes of Cip&MT-lips and Man-Cip&MT-lips are 112.20 ± 5.01 nm and 125.26 ± 4.34 nm. (C) Potential distribution of different liposomes. The Zeta potentials of Cip&MT-lips and Man-Cip&MT-lips are −6 ± 0.43 mV and −5.24 ± 0.48 mV. (D) Fourier infrared spectra of different components. (E) Transmission electron microscopy of different liposomes Data are presented as mean ± SD (n = 3); *p < 0.05, **p < 0.01, ***p < 0.001.

observe the pathological changes at the infected sites across the three different infection depths. Masson and Sirius red staining were utilized to examine changes in muscle and collagen expression at the infection sites in the skin and muscle of the infected mice. Immunofluorescence staining was conducted to assess the expression of MMP-9 and NF-κB-p65 at the infection sites in the three different depth infection models. Kaplan-Meier survival curves were plotted for mice throughout the treatment process, and daily body weight changes of the mice were recorded after drug administration. ELISA detection kits were employed to investigate the expression of inflammatory factors IL-1β, TNF-α, and IL-6 in the blood of the mice.

2.14. Evaluation of formulation safety

Saline, Cip, Cip&MT, CIP&MT-lips, and Man-CIP&MT-lips were administered via tail vein injection to healthy BALB/c mice according to treatment protocols for bacterial infections. On the day following the last administration, blood was collected from each group of mice, and the mice were subsequently euthanized. The organs were harvested for embedding and sectioning. HE staining was employed to observe pathological changes in the organs. A complete blood analyzer was used to determine the number of immune cells in the blood of mice treated with Man-CIP&MT-lips, and this was compared with the physiological saline group. A hemolysis assay was conducted to evaluate the hemolytic effect of Man-CIP&MT-lips. Man-CIP&MT-lips at different mass concentrations were co-incubated with a 2% red blood cell suspension at 37 °C for 2 h, with saline serving as the negative control and distilled water as the positive control. Following centrifugation at 3000 rpm for 5 min, the supernatant was collected to measure absorbance at 540 nm and calculate the hemolysis rate. The cytotoxicity of Man-CIP&MT-lips on RAW264.7 and A549 cells was determined using the SRB method. Cells were seeded in 96-well plates at a concentration of 1×10^4 cells/well. When the cells reached 50% confluence, Man-CIP&MT-lips at concentrations of 100, 50, 25, 12.5, 6.25, 3.125, and 1.5625 μg/mL were added to the wells. After 48 h of incubation, the SRB method was utilized to assess cytotoxicity.

2.15. Data analysis

Data analysis was conducted using GraphPad Prism 9 software (IBM, USA). Differences between groups were assessed using a one-way ANOVA test. All data are presented as mean ± standard deviation (mean ± SD), with $p < 0.05$ considered statistically significant.

3. Results and discussion

3.1. Characterization of liposomes

The characterization results of the liposomes are presented in Fig. 2. The apparent images of various liposomes are displayed in Fig. 2A. When illuminated from one side of the vial, the laser creates a bright path through the solution, exiting from the opposite side. The formation of liposomes transforms the solution into a colloidal suspension, and the laser illumination induces the Tyndall effect. This result suggests that the solution contains colloidal particles [27]. The EE of Cip and MT in liposomes was 88.38 ± 2.47 % and 89.28 ± 7.66 %, respectively. Both Cip and MT exhibited high EE. This efficient encapsulation is primarily attributed to the successful application of the ammonium sulfate gradient method and the thin-film dispersion method. As an alkaloid, MT's lipid-water partition properties suggest that it may preferentially associate with the lipid bilayer. Meanwhile, the ammonium sulfate gradient method allows Cip is presumed to be captured and stabilized in

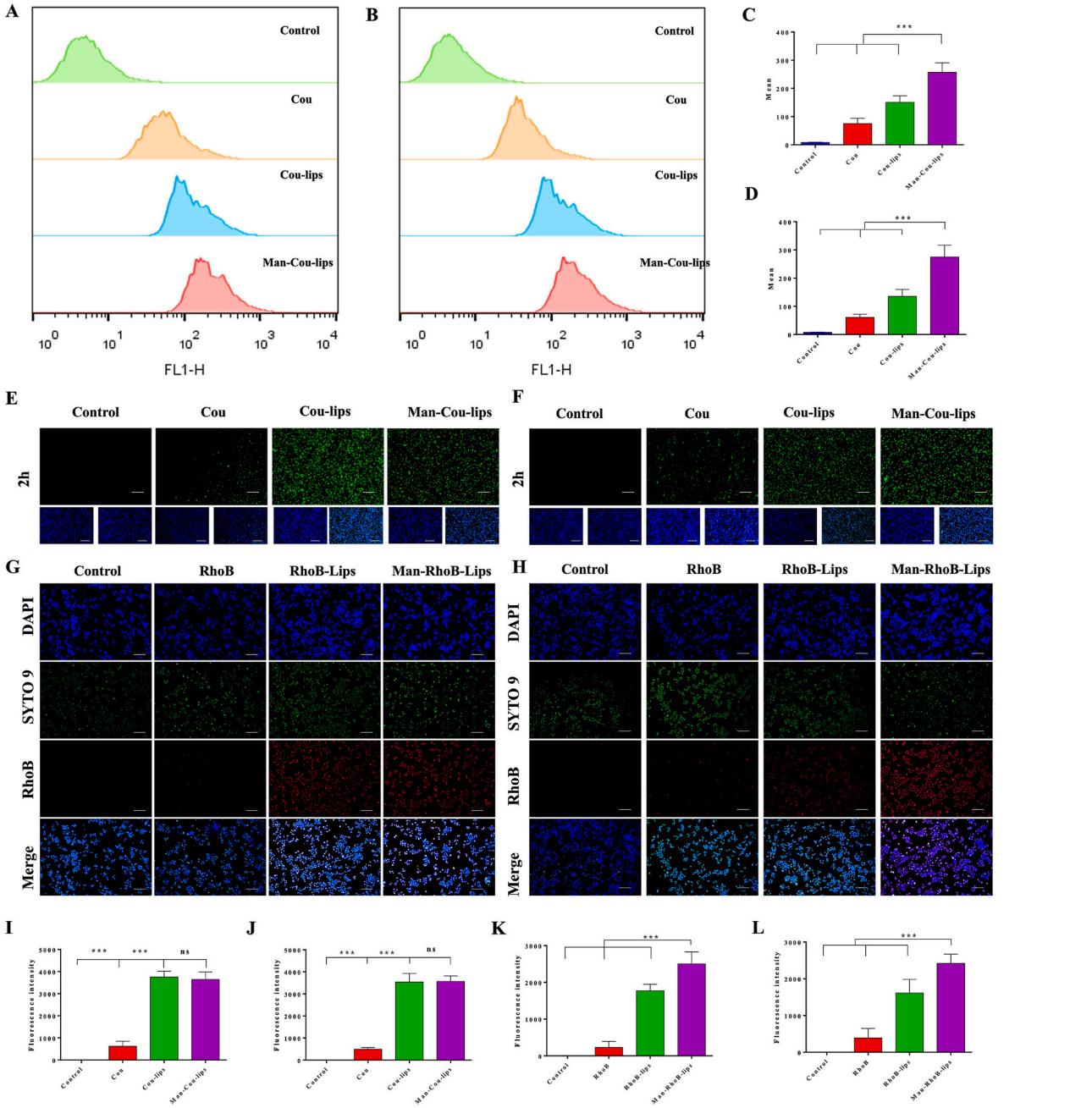


Fig. 3. Uptake of liposomes by bacteria and cells. (A-B) Flow cytometry analysis of coumarin uptake by MRSA (A) and *Pseudomonas aeruginosa* (B)-infected RAW264.7 cells. (C-D) Quantitative statistics of coumarin uptake by MRSA (C) and *Pseudomonas aeruginosa* (D)-infected RAW264.7 cells detected via flow cytometry. (E-F) Fluorescence microscopy observation of coumarin uptake by MRSA (E) and *Pseudomonas aeruginosa* (F). (G-H) Fluorescence microscopy observation of coumarin uptake by MRSA (G) and *Pseudomonas aeruginosa* (H)-infected RAW264.7 cells. (I-L) Quantitative statistical results of E(I), F(J), G(K), and H(L). The data are presented as mean ± SD (n = 3); *p < 0.05, **p < 0.01, ***p < 0.001.

the aqueous core of liposomes through active drug loading. Consequently, both drugs with distinct physicochemical properties achieved and maintained high encapsulation efficiency. Representative results of particle size and potential distribution of Cip&MT-lips and Man--Cip&MT-lips are shown in Fig. 2B and C. The particle size of Cip&MT-lips is 112.20 ± 5.01 nm, while the potential is −6.00 ± 0.43 mV. For Man-Cip&MT-lips, the particle size is 125.26 ± 4.34 nm, with a potential of −5.24 ± 0.48 mV. The PDI of both Cip&MT-lips (17.83 ± 0.84 %) and Man-Cip&MT-lips (19.16 ± 1.37 %) was less than 0.2, indicating that the particle size distribution of liposomes was uniform and the system was stable. The slight increase in particle size and the change in Zeta potential are consistent with the insertion of DSPE-PEG_{2000}-Man into the liposome bilayer, although direct structural confirmation was not performed in this study. Upon entering the organism, liposomes with smaller particle sizes exhibit a longer circulation time in vivo, are more likely to penetrate the gaps in the vascular endothelium, and can effectively reach inflammatory sites [28,29]. Here, they may be recognized and internalized by local macrophages, thereby increasing the drug concentration in the target tissue and enhancing the therapeutic effect. The Fourier infrared spectra results for the different liposomes are illustrated in Fig. 2D. Cip and MT exhibit characteristic absorption peaks at 1700 and 1680 cm^{-1}, respectively [30,31]. However, after encapsulation within the liposomes, these characteristic peaks weaken or disappear, supporting the

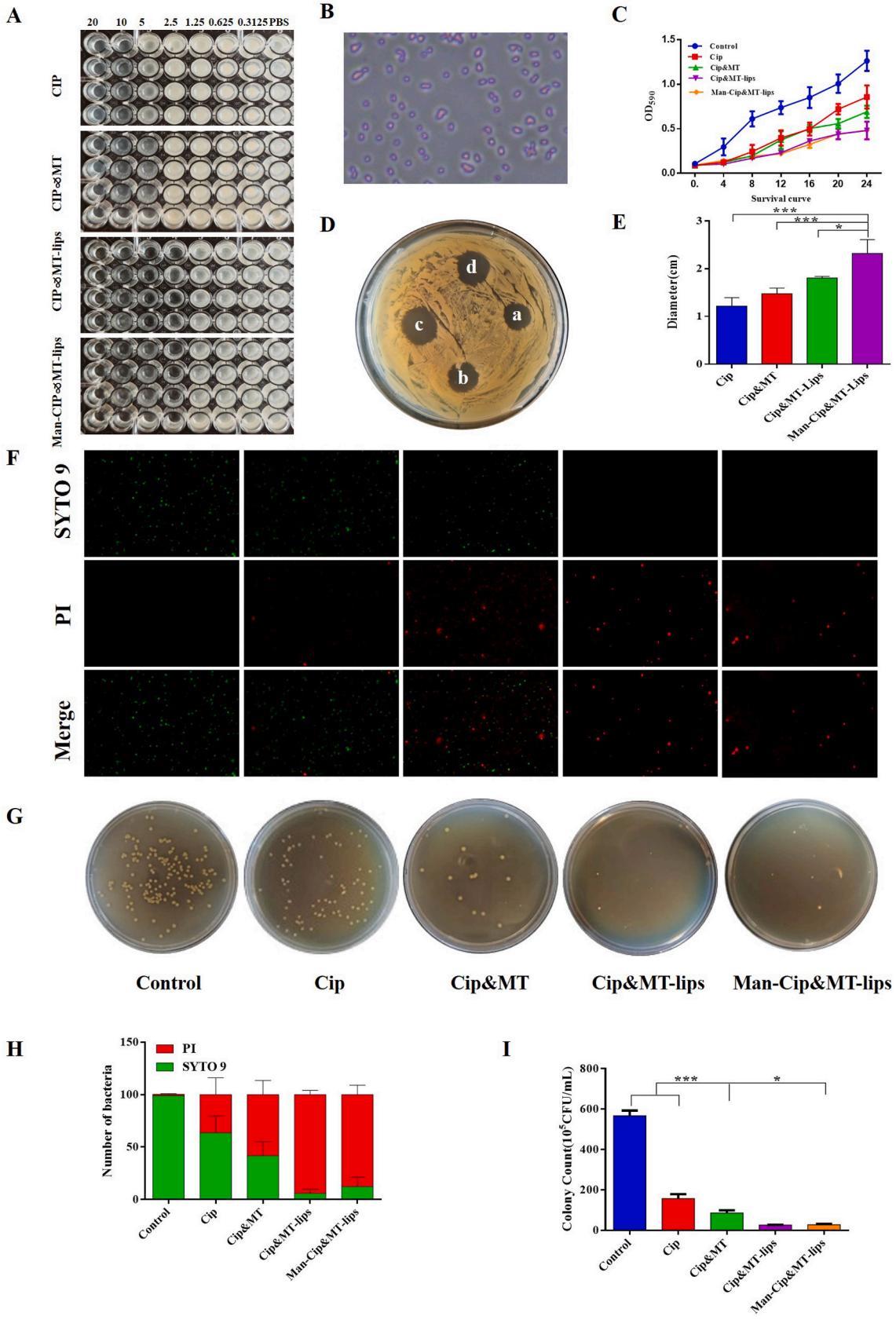


Fig. 4. Detection of antibacterial activity of MRSA. (A) MIC values of MRSA in different preparation groups. (n = 4) (B) Gram stain for MRSA (C) Bacterial growth curves after treatment with different preparations. (D-E) Antibacterial zone and antibacterial zone diameter of different preparations. (F) LIVE/DEAD staining of bacteria treated with different preparations. (G) Colony count after treatment of different preparation groups (H) Statistics of LIVE/DEAD relative fluorescence intensity. (I) Statistics of colony counts. Data are presented as mean ± SD (n = 3); *p < 0.05, **p < 0.01, ***p < 0.001.

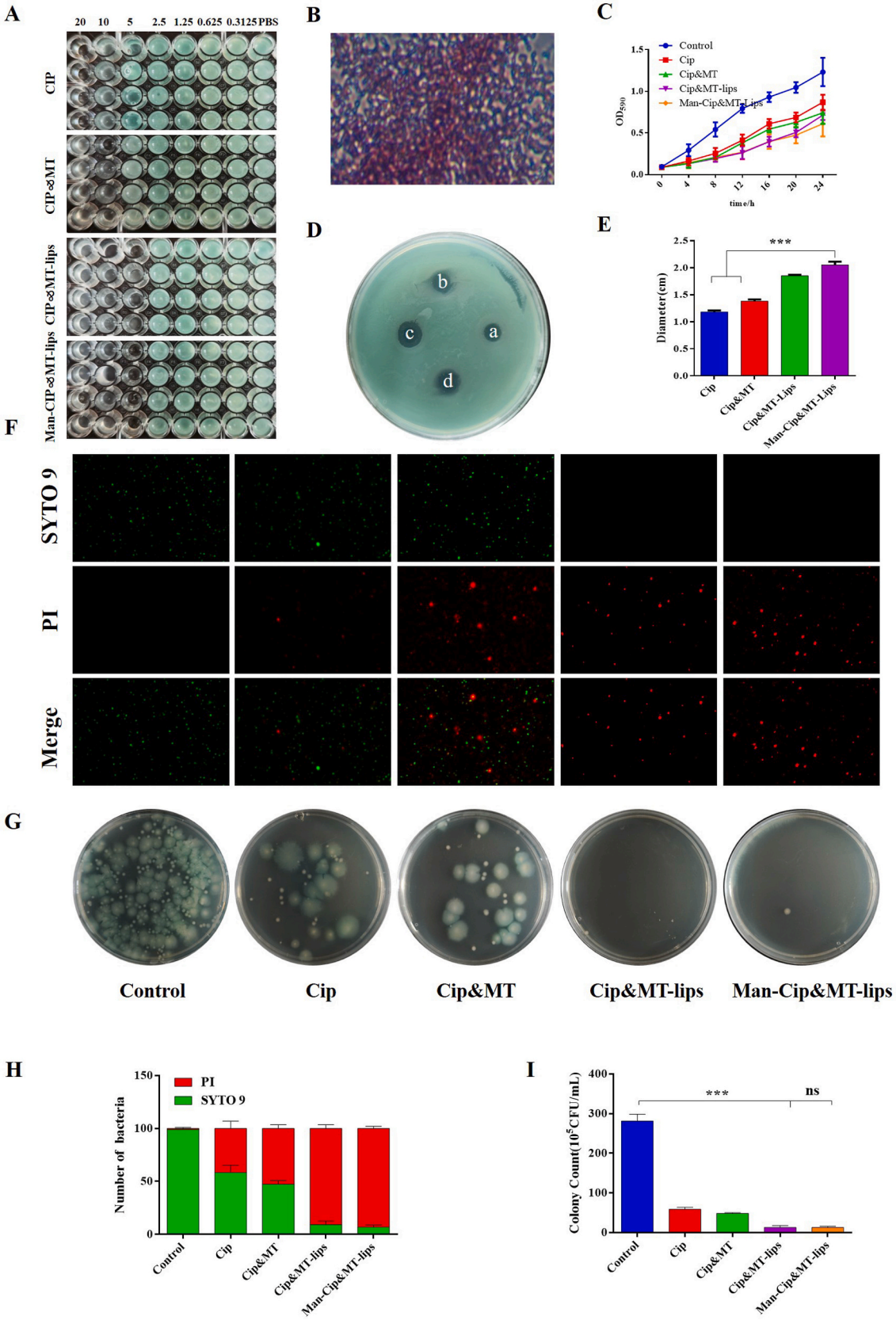


Fig. 5. Detection of antibacterial activity of *Pseudomonas aeruginosa*. (A) MIC values of *Pseudomonas aeruginosa* in different preparation groups. (n = 4) (B) Gram stain for *Pseudomonas aeruginosa*. (C) Bacterial growth curves after treatment with different preparations. (D-E) Antibacterial zone and antibacterial zone diameter of different preparations. (F) LIVE/DEAD staining of bacteria treated with different preparations. (G) Colony count after treatment of different preparation groups (H) Statistics of LIVE/DEAD relative fluorescence intensity. (I) Statistics of colony counts. Data are presented as mean ± SD (n = 3); *p < 0.05, **p < 0.01, ***p < 0.001.

successful encapsulation of the two drugs within liposomes. The drug molecules are presumed to be localized either within the internal aqueous phase or associated with the phospholipid bilayer, based on the preparation method and their physicochemical properties, although this distribution was not directly verified in the present study. This physical entrapment significantly restricts the free vibration and rotation of C=O bonds in the drug molecules, thereby resulting in the disappearance of the characteristic peaks. The TEM results of Cip&MT-lips and Man--Cip&MT-lips are presented in Fig. 2E. The liposomes exhibit structurally intact vesicles with well-defined boundaries, displaying both spherical and elliptical shapes. The regularity of these morphologies indicates the successful formation of structurally intact vesicles. The appearance of elliptical structures is likely due to natural deformation and collapse of the liposomes onto the grid during sample preparation and drying. This is a common phenomenon observed with flexible lipid nanoparticles in TEM imaging and does not affect our core conclusion regarding their successful formation as intact vesicular structures. Following Man modification, the fundamental structural characteristics of Cip&MT-lips were preserved, exhibiting a more uniform size distribution and a more stable aggregation state. This observation is attributed to the influence of DSPE-PEG_{2000}-Man addition on the preparation process and properties of the liposomes. To ensure the reliability and comparability of all fluorescently labeled liposomes in subsequent targeting and distribution studies, we characterized the Cou-, RhoB-, and DiR-labeled liposomes. All formulations exhibited uniform nanoparticle sizes similar to drug-loaded liposomes, low PDI, and comparable zeta potentials (Supplementary Table S1). These results indicate the high reproducibility of our preparation process and demonstrate that the fluorescent labeling procedure does not significantly affect the critical physicochemical properties of liposomes, thereby ensuring the reliability of subsequent biological experimental results. The liposomes exhibited slight aggregation during long-term storage, which is a common phenomenon in nanoformulations. However, within the first two weeks, the changes in particle size and PDI remained relatively mild, indicating that the formulation maintained good physical stability within a reasonable storage period (Supplementary Table S2). Additionally, the liposomes demonstrated excellent colloidal stability in serum, with their surface PEG layer effectively delaying serum protein-induced aggregation (Supplementary Table S3). These stability data indicate that Man--Cip&MT-lips exhibit outstanding stability during the critical time window required for exerting pharmacological effects in physiological environments.

3.2. Evaluation of in vitro targeting of liposomes

The in vitro targeting evaluation results of liposomes are presented in Fig. 3. Since neither Cip nor MT exhibits intrinsic fluorescence, Cou was encapsulated within the liposomes as a fluorescent probe to enable visualization and quantitative analysis [32]. The flow cytometry results depicting the uptake of different liposomes by RAW264.7 cells infected with MRSA or *Pseudomonas aeruginosa* are illustrated in Fig. 3A–D. Cells infected with bacteria exhibited minimal uptake of free Cou. In contrast, when Cou was encapsulated within liposomes, cellular uptake was significantly increased. Furthermore, after mannose modification, the uptake of liposomes by RAW264.7 cells was further enhanced compared to unmodified liposomes. The higher intracellular fluorescence intensity observed in the Man-Cou-lips group compared to the Cou-lips group suggests enhanced cellular uptake. This enhancement may be associated with mannose receptor-mediated endocytosis, which has been widely reported as a potential uptake pathway for mannosylated carriers in macrophages.

Fig. 3E–F, I–J, and S1 present the evaluation of liposome interactions with MRSA or *P. aeruginosa*. Encapsulation of Cou in liposomes effectively improved the uptake of the hydrophobic probe compared to the free Cou group. However, no significant difference was observed between the Cou-lips and Man-Cou-lips groups in terms of bacterial uptake. This phenomenon may be related to the fact that mannose receptors are primarily expressed on immune cells such as macrophages. When Man-modified liposomes were co-incubated with bacteria, the lack of significant difference in uptake suggests the absence of specific recognition sites on the bacterial surface, resulting in comparable uptake behavior between modified and unmodified liposomes.

To further visualize the targeting behavior of liposomes toward intracellularly infected cells, fluorescence microscopy was employed. MRSA or *P. aeruginosa* was first labeled with SYTO-9, a membrane-permeable nucleic acid dye that enhances fluorescence upon binding to bacterial nucleic acids, enabling live bacteria to emit green fluorescence [33]. After establishing the intracellular infection model in RAW264.7 cells, the uptake of liposomes was evaluated (Fig. 3G–H, K–L). Consistent with the flow cytometry results, encapsulation of RhoB within liposomes resulted in a significant increase in intracellular red fluorescence intensity. Moreover, mannose modification further enhanced liposome uptake by macrophages compared to unmodified liposomes.

Overall, the in vitro targeting evaluation results suggest that mannose-modified liposomes exhibit improved uptake in RAW264.7 cells infected with bacteria, supporting their potential application for targeted intracellular drug delivery.

3.3. Determination of minimum inhibitory concentration

After successfully constructing Man-Cip&MT-lips and determining their targeting ability, we evaluated their pharmacological efficacy in vitro. Figs. 4 and 5 illustrate the inhibitory effects of Man-Cip&MT-lips on MRSA and *P. aeruginosa*, respectively. The MIC of free CIP against MRSA or *P. aeruginosa* was 5 μg/ml (Figs. 4A–5A). When MT and CIP were used in combination, the MIC for both bacteria decreased to 2.5 μg/ml, indicating a synergistic antibacterial effect between CIP and MT. Furthermore, when CIP and MT were encapsulated in liposomes, the MIC decreased further to 1.25 μg/ml. The limited water solubility of CIP adversely affected its therapeutic efficacy. However, encapsulating CIP in liposomes significantly increased its solubility, allowing for a lower dose to achieve the desired therapeutic effect. Notably, after Man modification, the MIC of Man-Cip&MT-lips remained at 1.25 μg/ml. This result can be attributed to the absence of mannose receptor expression on the bacterial surface, a phenomenon that is consistent with the findings from the targeting investigation. The Gram staining results indicated that MRSA appeared purple (Fig. 4B), while *P. aeruginosa* exhibited a reddish hue (Fig. 5B), thereby preliminarily confirming the presence of both MRSA and *P. aeruginosa*.

3.4. Dynamic observation of bacterial growth

We measured the OD values of bacteria at different time points during growth to plot the time-growth curves, thereby understanding the growth characteristics of the bacteria. The time-growth curves for MRSA and *P. aeruginosa* are shown in Figs. 4C–5C. During the first 0-2 h, the bacteria were in a lag phase, with relatively stable OD values. After adapting to the new culture environment, the bacteria entered the exponential growth phase between 2 and 10 h. The OD values of the control group exhibited a linear increase, indicating that the bacteria were growing at an exponential rate. Following drug treatment, bacterial growth was inhibited, and the slope of the curve significantly decreased. During the stable phase from 8 to 24 h, the bacterial growth in the CIP&MT-lips and Man-CIP&MT-lips groups tended to stabilize, while the Control, Cip, and Cip&MT groups continued to show an upward trend. The plotting of the time-growth curves allows for a visual observation of the inhibitory effects of CIP&MT-lips and Man-CIP&MT-lips on the growth of MRSA and *P. aeruginosa*.

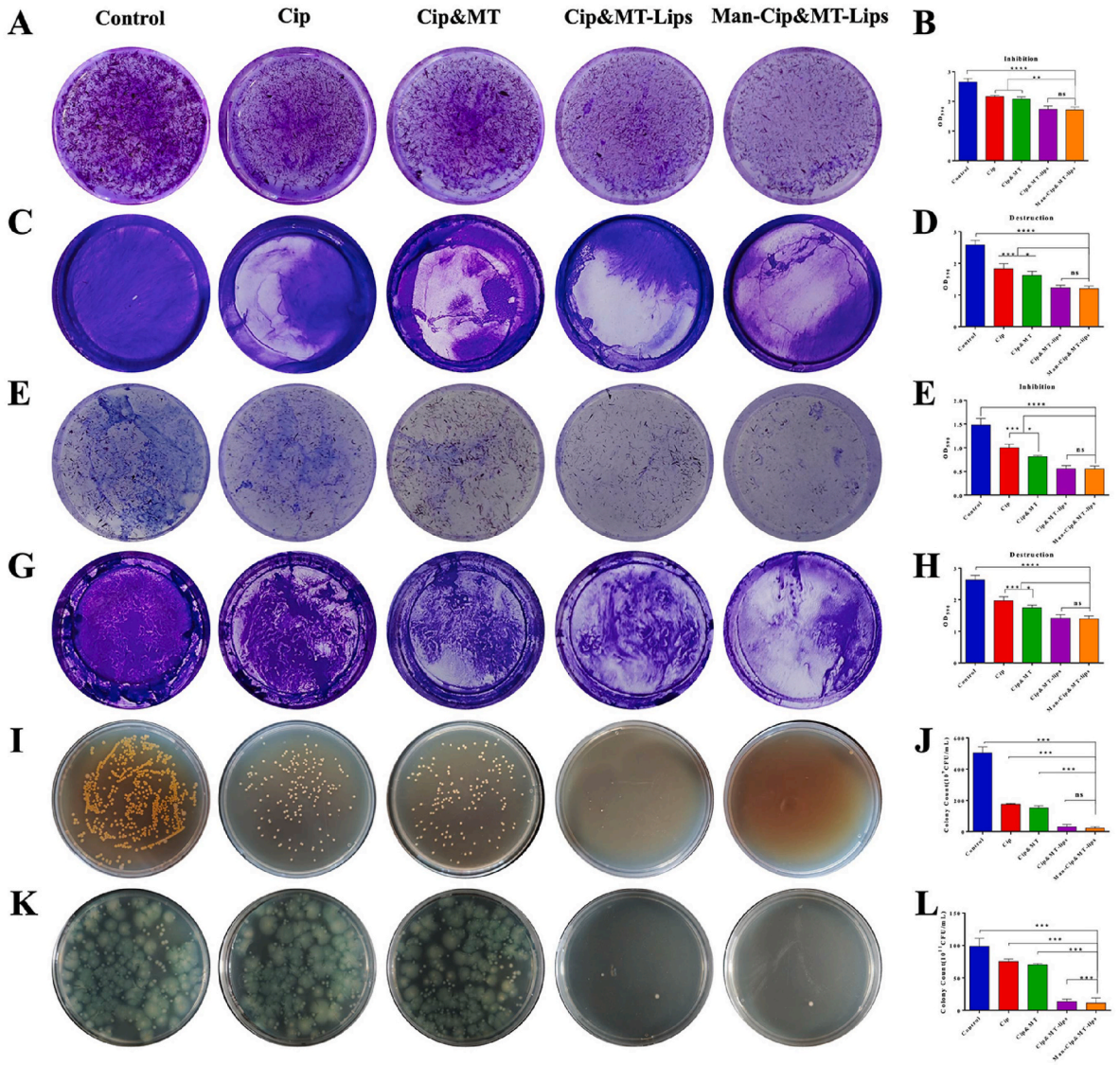


Fig. 6. Determination of biofilm inhibitory effects (A-B) Inhibitory effects of different formulations on MRSA biofilm formation; (C-D) Eradication effects of different formulations on MRSA biofilms; (E-F) Inhibitory effects of different formulations on *Pseudomonas aeruginosa* biofilm formation; (G-H) Eradication effects of different formulations on *Pseudomonas aeruginosa* biofilms; (I-J) Colony counts of MRSA biofilms treated with different formulations; (K-L) Colony counts of *Pseudomonas aeruginosa* biofilms treated with different formulations. Data are presented as mean ± SD (n = 3); *p < 0.05, **p < 0.01, ***p < 0.001.

3.5. The zone of inhibition test

The antibacterial circle experiment is a commonly used method for assessing the efficacy of antibiotics [34]. After diffusion on solid LB agar, antibiotics create a concentration gradient from high to low. When the antibiotic concentration at the edge of the agar reaches the MIC, bacterial proliferation ceases, resulting in a specific size of the inhibition zone to evaluate the antibacterial activity of the antibiotic. The results of the inhibition zone experiments for various drug groups against MRSA or *P. aeruginosa* are shown in Fig. 4D and E and 5D-E. The diameters of the inhibition zones for the Cip, CIP&MT, Cip&MT-lips, and Man-Cip&MT-lips groups against MRSA were 1.22 ± 0.18, 1.47 ± 0.12, 1.81 ± 0.03, and 2.32 ± 0.29 cm, respectively; against *P. aeruginosa*, the diameters were 1.18 ± 0.03, 1.38 ± 0.03, 1.85 ± 0.02, and 2.05 ± 0.06 cm, respectively. Compared to the Cip&MT-lips group, the Man-Cip&MT-lips group exhibited a significantly enhanced inhibitory effect against MRSA, and also showed inhibitory effects on *P. aeruginosa*, although the effect was not significant. Man-Cip&MT-lips may have a higher sensitivity against MRSA.

3.6. Bacterial live/dead staining

The results of live-dead bacterial staining for each group of drugs against MRSA or *P. aeruginosa* are shown in Fig. 4F, H, 5F, and 5H. The live-dead bacterial staining kit contains two fluorescent probes, SYTO-9 and PI [35]. SYTO-9 is a nucleic acid dye that labels live bacteria green [36]. PI binds to double-stranded DNA in damaged cell membranes and emits red fluorescence [37]. The ratio of live to dead bacteria can be determined by observing the amounts of green and red fluorescence. In the Control, Cip, CIP&MT, Cip&MT-lips, and Man-Cip&MT-lips groups, the number of bacteria exhibiting green fluorescence gradually decreased, while conversely, the number of bacteria exhibiting red fluorescence gradually increased. The treatment with the drugs demonstrated a bactericidal effect; however, the modification with Man did not enhance this effect.

3.7. Post-treatment colony count

The results of bacterial plating after drug treatment are shown in Fig. 4G, I, 5G, and 5I. The Control group exhibited a large number of

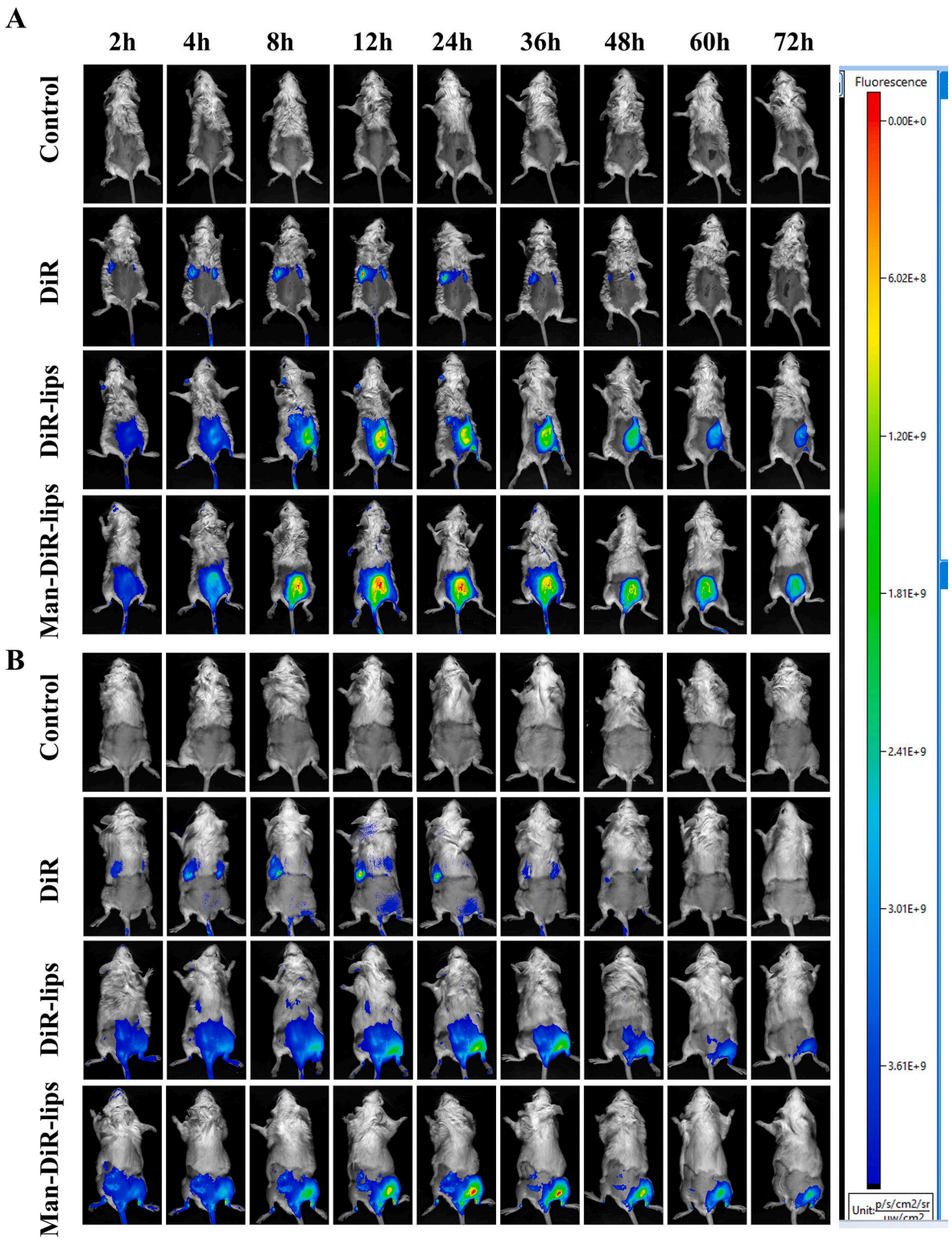


Fig. 7. In vivo distribution of DiR in different formulations. (A) In vivo distribution in skin-infected mice. (B) In vivo distribution in muscle-infected mice.

bacterial colonies in the culture dishes, indicating that bacteria can grow and reproduce normally in the absence of drug treatment. From the Cip group to the Cip&MT group, the antibacterial effect gradually increased. Furthermore, encapsulating the drugs in liposomes, particularly in Man-modified liposomes, demonstrated a more significant antibacterial effect. The combined use of Cip and MT exhibited a synergistic antibacterial action, with liposomes serving as drug carriers that effectively protect the drugs, prolong their action time, and enhance their concentration at the site of infection. Man-modified liposomes further improved the targeting of the drugs, achieving a more efficient antibacterial effect.

3.8. Investigation of biofilm inhibition

Biofilms are complex community structures formed by bacteria through the extracellular secretion of polysaccharides, proteins, and

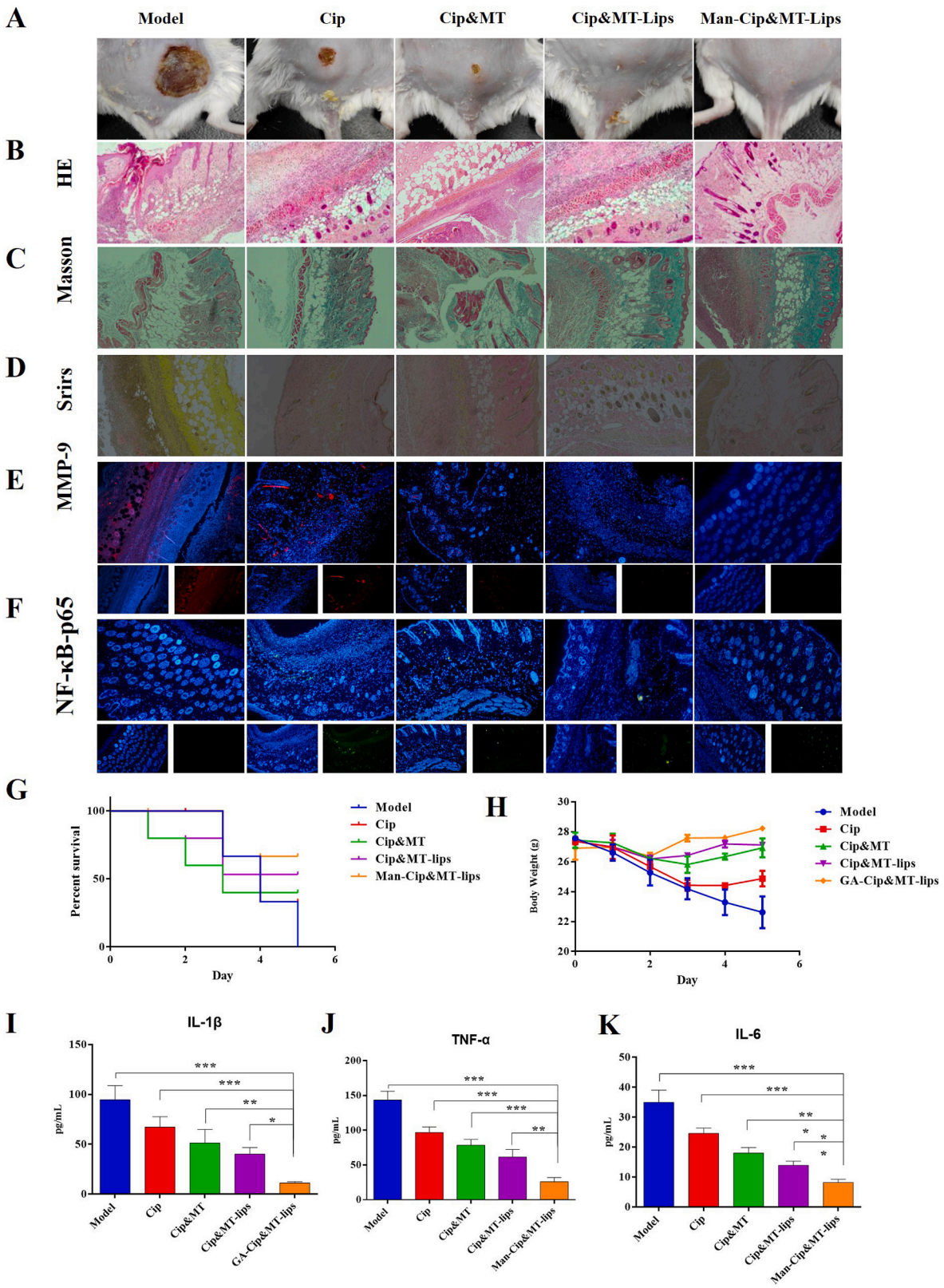


Fig. 8. Evaluation of therapeutic effect of different formulations on mice with skin infection (A) Skin images of mice with skin infection after different treatments. (B) HE staining of skin infected mice after different treatments. (C) Masson staining of skin infected mice after different treatments. (D) The skin of infected mice was stained with Sirius red after different treatments. (E) MMP-9 immunofluorescence staining of skin infected mice after different treatments. (F) NF-kβ-p65 immunofluorescence staining of skin infected mice after different treatments. (G) Survival curve of mice within 5 days of administration. (H) Weight change curve of mice within 5 days of administration (I-K) The expression levels of IL-1β, TNF-α and IL-6 in different treated mice were measured. Data are presented as mean ± SD (n = 6); *p < 0.05, **p < 0.01, ***p < 0.001. (For interpretation of the references to color in this figure legend, the reader is referred to the Web version of this article.)

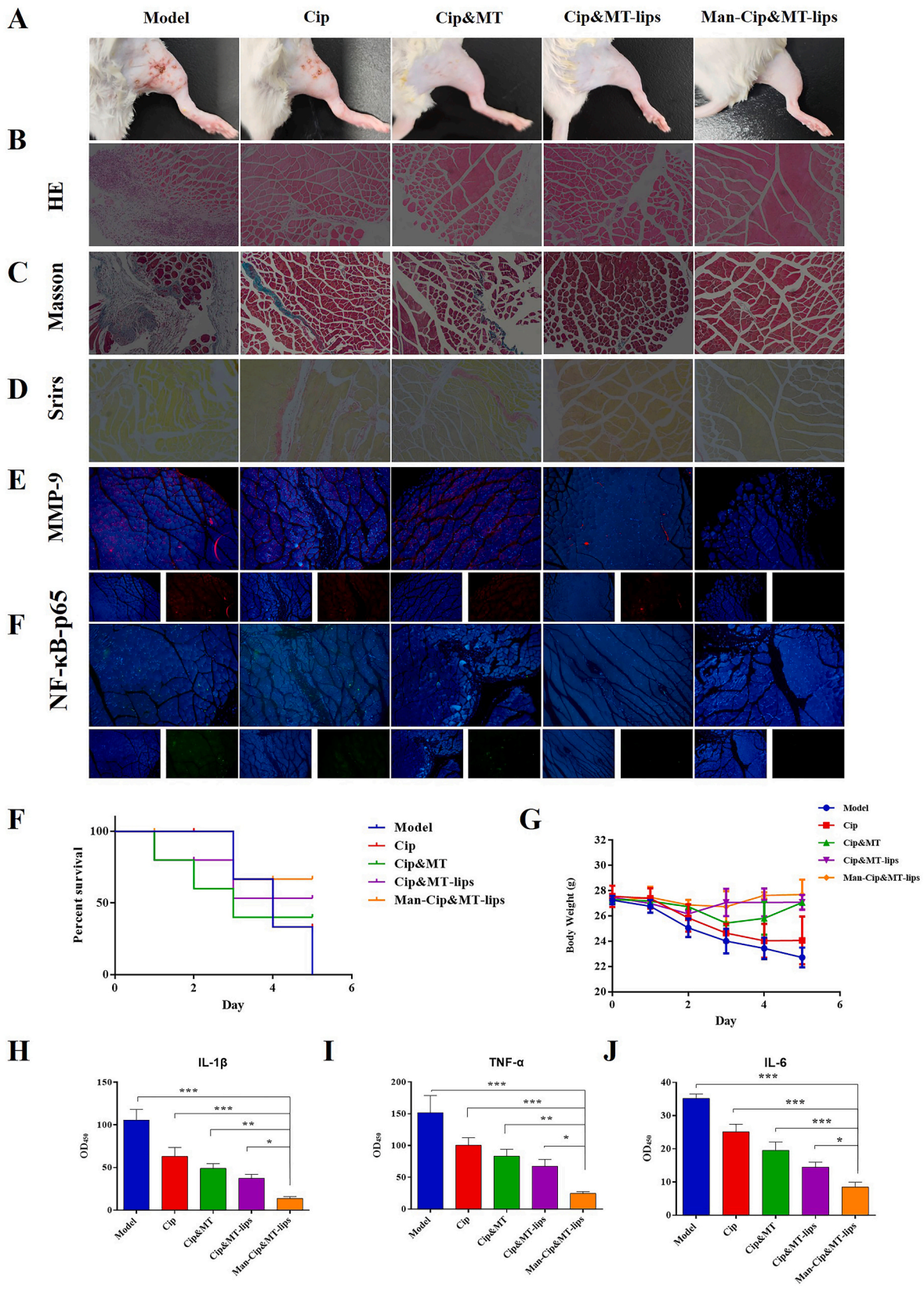


Fig. 9. Evaluation of therapeutic effect of different formulations on mice with muscle infection (A) Different preparations treated muscle pictures of mice with muscle infection. (B) HE staining of muscle infected mice with different preparations. (C) Muscular-infected mice were stained with masson by different preparations. (D) Sirian red staining of muscle in mice with muscle infection was observed with different preparations. (E) Immunofluorescence staining of MMP-9 in muscle infected mice with different preparations (F) Immunofluorescence staining of NF-kβ-p65 in muscle infected mice with different preparations(G) Survival curve of mice within 5 days of administration. (H) Weight change curve of mice within 5 days of administration (I-K) The expression levels of IL-1β, TNF-α and IL-6 in different treated mice were measured. Data are presented as mean ± SD (n = 6); *p < 0.05, **p < 0.01, ***p < 0.001. (For interpretation of the references to color in this figure legend, the reader is referred to the Web version of this article.)

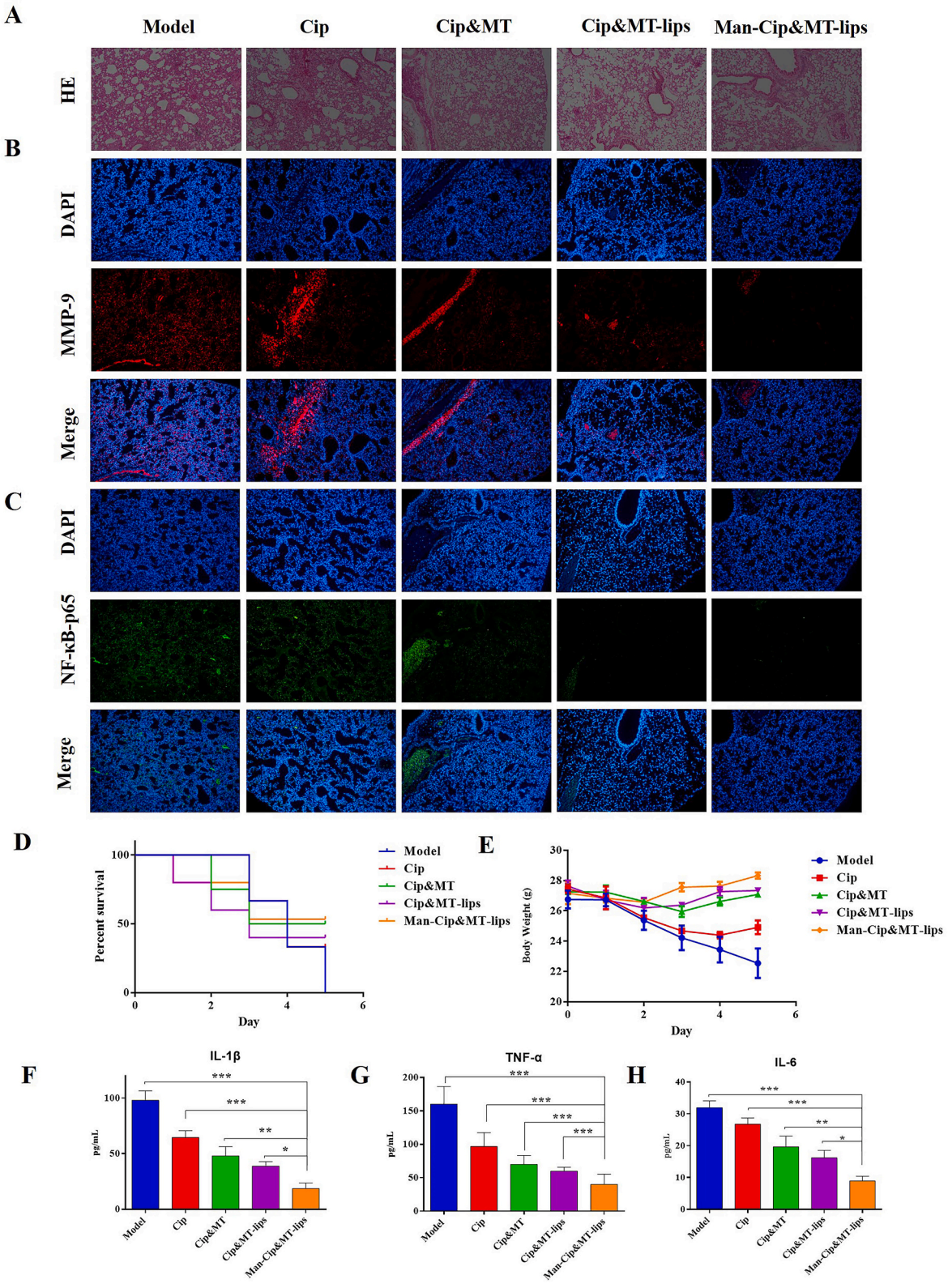


Fig. 10. Therapeutic effects of different preparations on mice with pulmonary infection. (A) HE staining of lung treated with different formulations. (B) Expression of MMP-9 in lung after treatment with different formulations. (C) Expression of pulmonary NF-kβ-p65 after treatment with different formulations. (D) Survival curve of mice within 5 days of administration. (E) Weight change curve of mice within 5 days of administration (F-H) The expression levels of IL-1β, TNF-α and IL-6 in different treated mice were measured. Data are presented as mean ± SD (n = 6); *p < 0.05, **p < 0.01, ***p < 0.001.

extracellular DNA, creating a cohesive network [38,39]. They represent a structure formed by bacterial populations that adhere to a specific substrate. Biofilms exhibit strong hydrophobicity, preventing the penetration of antibiotics and the infiltration of immune cells through electrostatic adsorption and physical shielding, leading to bacterial resistance [40,41]. Furthermore, biofilms can induce bacterial metabolic dormancy, stress responses, and quorum sensing, or upregulate the expression levels of bacterial efflux pumps, further increasing resistance and resulting in severe consequences such as local inflammation, chronic infections, and organ failure or death [42,43]. Using crystal violet staining, the distribution of MRSA biofilms was observed during the formation phase (Fig. 6A and C) and maturation phase (Fig. 6B and D) [44]. Drug intervention during the biofilm formation phase can effectively prevent its development. When MT is used in conjunction with Cip, the biofilm color lightens compared to the Cip group. Encapsulating the drug in liposomes significantly enhances this inhibitory effect. For mature biofilms, after treatment, the distribution of the biofilm becomes increasingly uneven, and the color diminishes. The effects of the CIP&MT-lips group and the Man-CIP&MT-lips group are comparable. A similar phenomenon was observed in the formation of *P. aeruginosa* biofilms at the mature stage, akin to that seen with MRSA. To quantitatively analyze the bacterial status in the biofilms post-treatment, we performed a plate coating experiment on the bacteria within the biofilms after drug treatment (Fig. 6I–L). Consistent with the results observed through crystal violet staining, the Control group still harbored a significant number of bacteria. The bacterial counts in the Cip and Cip&MT groups gradually decreased. The CIP&MT-lips and Man-CIP&MT-lips groups exhibited the lowest bacterial counts, effectively inhibiting the formation of MRSA or *P. aeruginosa* biofilms.

3.9. Evaluation of the in vivo targeting ability of liposomes

In clinical treatment, bacterial infections often occur in areas such as the skin, mucous membranes, muscles, tissues, and organs. Infection sites at different depths typically exhibit distinct vascular densities and blood supply characteristics, which can influence the distribution and delivery efficiency of nanocarriers in vivo [45,46]. To investigate the in vivo targeting behavior of Man-CIP&MT-lips, a “shallow-to-deep” bacterial infection model was established.

DiR was selected as a fluorescent probe for in vivo imaging. The targeting behavior of Man-DiR-lips in mice with skin and muscle infections is shown in Fig. 7. Due to its relatively low solubility and limited effective concentration, free DiR was not clearly detected at the infection site after 48 h. In contrast, when DiR was encapsulated within liposomes, the fluorescence signal at the infection site was prolonged, with detectable retention exceeding 72 h, indicating that liposomal encapsulation may extend the in vivo circulation time and improve local retention.

At 72 h, fluorescence signals from Man-DiR-lips were also observed at the infection site, with significantly higher intensity compared to DiR-lips. This result suggests that mannose modification may enhance the accumulation of liposomes at infected sites. This enhanced accumulation may be related to increased uptake by macrophages at infection sites, which are known to express mannose receptors, although this mechanism was not directly verified in the present study.

Overall, these in vivo imaging results suggest that mannose-modified liposomes exhibit improved accumulation at infection sites, which is consistent with the enhanced cellular uptake observed in the in vitro targeting studies.

3.10. In vivo therapeutic efficacy evaluation

We investigated the in vivo therapeutic effects of various drug groups on a "shallow to deep" infection model involving the skin, muscle, and lungs. At the end of the treatment period, the skin of the Model group mice still exhibited purulence, while the skin of the Man-Cip&MT-lips group mice had returned to a healthy state (Fig. 8A). Histological examination (HE staining) revealed a significant infiltration of inflammatory cells in the skin tissue of the Model group mice. After treatment, the infiltration of inflammatory cells gradually decreased, with the most notable reduction observed in the Man-Cip&MT-lips group (Fig. 8B). Masson's trichrome staining indicated that collagen fibers stained blue, while cytoplasm and red blood cells appeared red, and cell nuclei were stained blue-purple. Sirius Red staining showed that muscle fibers appeared yellow, and collagen fibers were red. Results from Masson staining (Fig. 8C) and Sirius Red staining (Fig. 8D) demonstrated that the number of intercellular collagen fibers in the liposome treatment group was significantly higher than that in the Model group. These results indicate that Man-Cip&MT-lips effectively inhibited inflammation at the infection site, and the tissue repair process is underway. Matrix metalloproteinases (MMPs) play a crucial role in the degradation and remodeling of the extracellular matrix, capable of degrading collagen and other matrix components, thereby influencing the degree of tissue fibrosis. NF-κB-p65 can induce the expression of various inflammatory factors in the body, promoting the occurrence and development of inflammatory responses. Immunofluorescence staining results show (Fig. 8E and F) that after treatment, the expression of MMP-9 and NF-κB-p65 in skin tissue was reduced, with the Man-Cip&MT-lips group showing the most significant decrease. During the treatment process, all mice in the Model group died by the fifth day (Fig. 8G); however, after treatment with Man-Cip&MT-lips, the survival rate of the mice reached 60%, and there was an upward trend in body weight (Fig. 8H). Additionally, the expression of inflammatory factors IL-1β, TNF-α, and IL-6 in serum was significantly reduced, indicating the effective therapeutic effect of Man-Cip&MT-lips (Fig. 8I–K).

The therapeutic effects of Man-Cip&MT-lips on muscle infections and pulmonary infections were investigated similarly. The results indicated that Man-Cip&MT-lips exhibited effects comparable to those observed in mice with skin infections for both muscle and pulmonary infections. In the Model group, the legs of the mice showed persistent redness and swelling, with joint flexion and mobility being restricted (Fig. 9A). After treatment, the symptoms alleviated, with the following order of relief: Man-Cip&MT-lips > Cip&MT-lips > Cip&MT > Cip. Histological staining results from HE, Masson, and Sirius Red (Fig. 9B–D) revealed that the Model group exhibited disorganized muscle structure, infiltration of inflammatory cells, increased deposition of collagen fibers, and some muscle fibers showing signs of rupture or dissolution. Following treatment, the tissue structure gradually returned to normal, with a reduction in inflammatory cell infiltration, decreased collagen fiber deposition, and normalization of muscle fiber expression. The most severely infected mice displayed pulmonary congestion along with significant inflammatory cell infiltration, which normalized after treatment (Fig. 10A). Post-treatment, the expression of MMP-9 and NF-κB-p65 in the tissues was suppressed (Fig. 9E and F, 10B-C), leading to improved survival rates in the mice, normalization of body weight, and a significant decrease in the expression of inflammatory factors in the blood (Fig. 9G–K, 10D-H).

Man-Cip&MT-lips exhibit a synergistic antibacterial effect in bacterial infections spanning “skin–muscle–lung” from superficial to deep tissues. Compared with Cip alone, the combination of Cip and MT demonstrated improved therapeutic efficacy, supporting the rationale for the co-administration of these two agents. Furthermore, encapsulation within liposomal nanocarriers further enhanced the therapeutic performance, which may be related to the sustained release behavior and improved in vivo retention of the drugs. Following systemic administration, the presence of a PEG hydration layer on the liposome surface may help reduce rapid clearance by the mononuclear phagocyte system, thereby prolonging circulation time. After mannose modification, the enhanced accumulation and cellular uptake observed in both in vitro and in vivo studies suggest that the liposomes may exhibit improved interaction with macrophages at infection sites. This effect may be associated with mannose receptor-mediated endocytosis, a

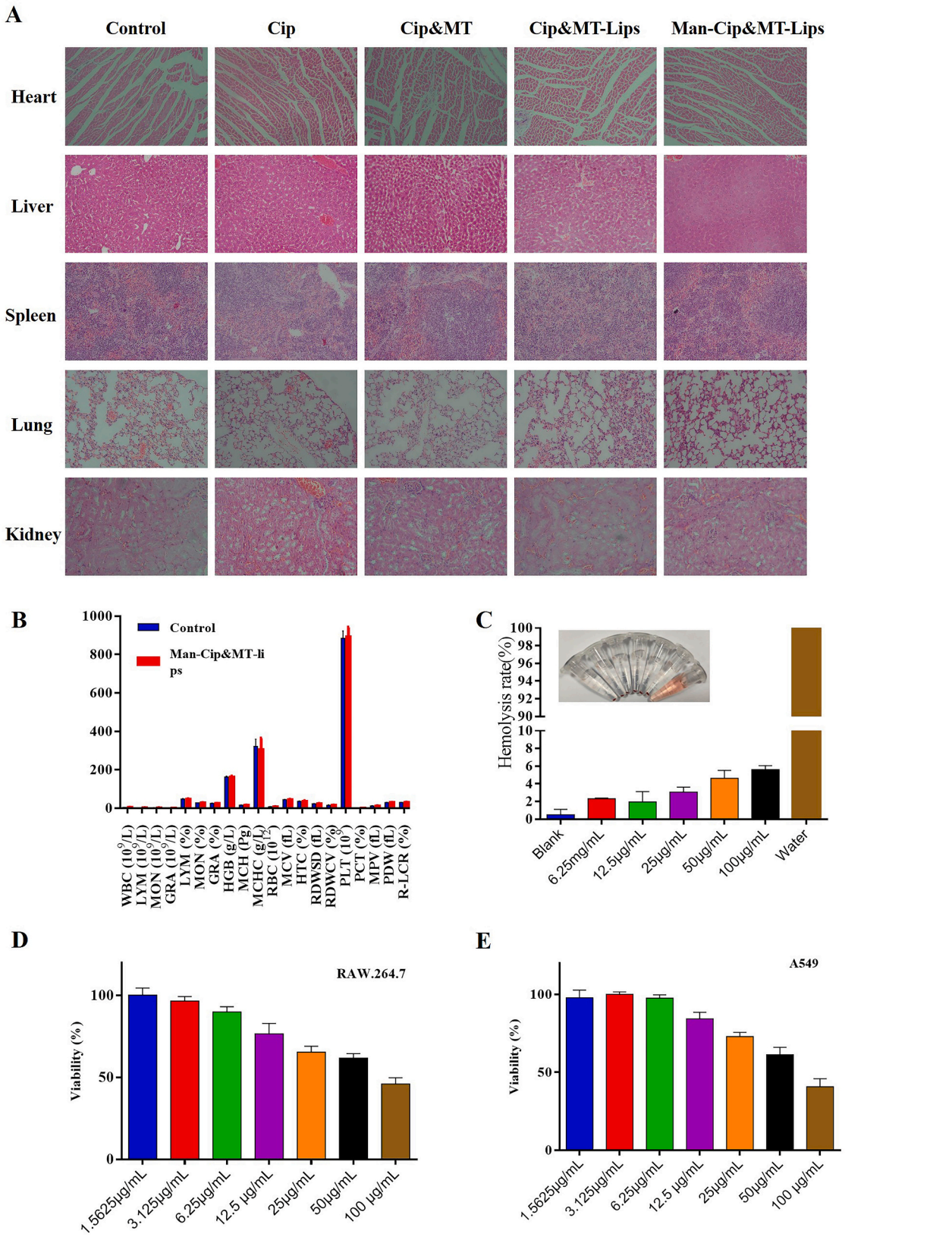


Fig. 11. Safety evaluation of preparation (A) HE staining of major organs of mice treated with different preparations. (B) Blood cell analysis after blank group and Man-Cip&MT-lips treatment. (C) Hemolysis behavior of GA-Cip&MT-lips at different concentrations. (D) Toxicity of Man-Cip&MT-lips at different concentrations to RAW 264.7 (E) Toxicity of GA-Cip&MT-lips at different concentrations to A549 cell line Data are presented as mean ± SD (n = 6); *p < 0.05, **p < 0.01, ***p < 0.001.

pathway widely reported for mannosylated nanocarriers, although this mechanism was not directly verified in the present study. Overall, these findings suggest that Man-Cip&MT-lips can enhance intracellular drug delivery and antibacterial efficacy, contributing to improved therapeutic outcomes against intracellular bacterial infections.

3.11. Evaluation of formulation safety

The results of histopathological examinations for each group are shown in Fig. 11A. The tissue structures of the heart, liver, spleen, lungs, and kidneys of the mice were all normal, with no obvious signs of cell necrosis or infiltration of inflammatory cells, and no significant pathological changes were observed. Blood analysis results indicate (Fig. 11B) that the levels of white blood cell count (WBC), red blood cell count (RBC), platelet count (PLT), hemoglobin (HGB), and others were all within the normal range, with no significant differences among the groups. The hemolysis rate of mice in each dosage group was below 5% (Fig. 11C), showing no significant difference compared to the blank control group, indicating that Man-CIP&MT-lips has a weak hemolytic effect on red blood cells and demonstrates good blood compatibility. Cytotoxicity test results show that Man-CIP&MT-lips exhibit low cytotoxicity to RAW264.7 and A549 cells, with cell viability remaining above 50% across the concentration range of 1.5625 μg/mL to 100 μg/mL. Man-CIP&MT-lips demonstrate good safety and have promising application prospects.

4. Conclusion

In this study, we developed a mannose-modified liposomal co-delivery system encapsulating Cip and MT. The prepared liposomes exhibited spherical morphology, uniform size distribution, and negative surface charge. In both in vitro and in vivo models, the mannose-modified liposomes demonstrated enhanced cellular uptake and improved therapeutic performance against intracellular bacterial infections under conditions of varying vascular density and blood supply. The co-delivery of Cip and MT resulted in a synergistic antibacterial effect, contributing to improved efficacy in bacterial clearance and biofilm inhibition. Overall, these findings suggest that Man-Cip&MT-lips may enhance intracellular drug delivery and improve the treatment of bacterial infections from superficial to deep tissues. This liposomal co-delivery strategy shows promising potential as a therapeutic approach for intracellular bacterial infections.

CRediT authorship contribution statement

Fangjin Lu: Software, Writing – original draft, Writing – review & editing. **Ping Mu:** Conceptualization, Funding acquisition. **Lin Zhu:** Supervision, Visualization. **SiTong Wang:** Data curation, Methodology. **Zhong Zhang:** Project administration, Resources. **Jiao Wang:** Resources, Writing – review & editing.

Declaration of competing interest

The authors declare that they have no known competing financial interests or personal relationships that could have appeared to influence the work reported in this paper.

Acknowledgments

This work was supported by the Education Department of Liaoning Province of China (LJ222410164013 to PM, LJ212410164008 to FL); Science and Technology Department of Liaoning Province of China (2024JH2/102600232 to PM); the Foundation of Spring Sunshine Program-Cooperative Research Project of the Ministry of Education (202200846 to PM)

Appendix A. Supplementary data

Supplementary data to this article can be found online at https://doi.org/10.1016/j.jddst.2026.108416.

Data availability

Data will be made available on request.

References

[1] J. Lu, X. Liu, X. Li, H. Li, L. Shi, X. Xia, B.L. He, T.F. Meyer, X. Li, H. Sun, X. Yang, Copper regulates the host innate immune response against bacterial infection via activation of ALPK1 kinase, Proc. Natl. Acad. Sci. U. S. A. 121 (2024) e2311630121, https://doi.org/10.1073/pnas.2311630121.
[2] S. Alven, B.A. Aderibigbe, Chitosan and cellulose-based hydrogels for wound management, Int. J. Mol. Sci. 21 (2020), https://doi.org/10.3390/ijms21249656.
[3] O. Henig, K.S. Kaye, Bacterial pneumonia in older adults, Infect. Dis. Clin. 31 (2017) 689–713, https://doi.org/10.1016/j.idc.2017.07.015.
[4] S.E. Woodward, L.M.P. Neufeld, J. Pena-Diaz, W. Feng, A. Serapio-Palacios, I. Tarrant, W. Deng, B.B. Finlay, Both pathogen and host dynamically adapt pH responses along the intestinal tract during enteric bacterial infection, PLoS Biol. 22 (2024) e3002761, https://doi.org/10.1371/journal.pbio.3002761.
[5] A.P. Kunnath, M. Suodha Suoodh, D.K. Chellappan, J. Chellian, K. Palaniveloo, Bacterial persister cells and development of antibiotic resistance in chronic infections: an update, Br. J. Biomed. Sci. 81 (2024) 12958, https://doi.org/10.3389/bjbs.2024.12958.
[6] C. Zhang, P.D. Straight, Antibiotic discovery through microbial interactions, Curr. Opin. Microbiol. 51 (2019) 64–71, https://doi.org/10.1016/j.mib.2019.06.006.
[7] S.M. Hosseini, M. Taheri, F. Nouri, A. Farmani, N.M. Moez, M.R. Arabestani, Nano drug delivery in intracellular bacterial infection treatments, Biomed. Pharmacother. 146 (2022) 112609, https://doi.org/10.1016/j.biopha.2021.112609.
[8] D.I. Duarte-Mata, M.C. Salinas-Carmona, Antimicrobial peptides immune modulation role in intracellular bacterial infection, Front. Immunol. 14 (2023) 1119574, https://doi.org/10.3389/fimmu.2023.1119574.
[9] Z. Abdullah, P.A. Knolle, Scaling of immune responses against intracellular bacterial infection, EMBO J. 33 (2014) 2283–2294, https://doi.org/10.15252/embj.201489055.
[10] S. Fillatreau, Novel regulatory functions for toll-like receptor-activated B cells during intracellular bacterial infection, Immunol. Rev. 240 (2011) 52–71, https://doi.org/10.1111/j.1600-065X.2010.00991.x.
[11] S. Yin, J. Yu, B. Hu, C. Lu, X. Liu, X. Gao, W. Li, L. Zhou, J. Wang, D. Wang, L. Lu, et al., Runx3 mediates resistance to intracellular bacterial infection by promoting IL12 signaling in group 1 ILC and NCR+ILC3, Front. Immunol. 9 (2018) 2101, https://doi.org/10.3389/fimmu.2018.02101.
[12] D.M. Campoli-Richards, J.P. Monk, A. Price, P. Benfield, P.A. Todd, A. Ward, Ciprofloxacin. A review of its antibacterial activity, pharmacokinetic properties and therapeutic use, Drugs 35 (1988) 373–447, https://doi.org/10.2165/00003495-198835040-00003.
[13] S. Bhatt, S. Chatterjee, Fluoroquinolone antibiotics: occurrence, mode of action, resistance, environmental detection, and remediation - a comprehensive review, Environ. Pollut. 315 (2022) 120440, https://doi.org/10.1016/j.envpol.2022.120440.
[14] K.H. Park, D. Kim, M. Jung, D.Y. Kim, Y.M. Lee, M.S. Lee, K.W. Hong, I.G. Bae, S. I. Hong, O.H. Cho, Effects of sub-inhibitory concentrations of nafcillin, vancomycin, ciprofloxacin, and rifampin on biofilm formation of clinical methicillin-resistant Staphylococcus aureus, Microbiol. Spectr. 12 (2024) e0341223, https://doi.org/10.1128/spectrum.03412-23.
[15] G.F. Zhang, X. Liu, S. Zhang, B. Pan, M.L. Liu, Ciprofloxacin derivatives and their antibacterial activities, Eur. J. Med. Chem. 146 (2018) 599–612, https://doi.org/10.1016/j.ejmech.2018.01.078.
[16] Y. Hu, X. Xu, J. Chen, T. Xu, P. Cui, R. Fan, Q. He, Identification of CH(2)-linker modified desfluoroquinolone-aminopyrimidine hybrids to combat antibiotic-resistant gram-positive bacteria, Bioorg. Chem. 161 (2025) 108496, https://doi.org/10.1016/j.bioorg.2025.108496.
[17] J. Zhao, Z. Gong, W. Bao, X. Liu, Z. Yu, Y.Q. Dong, W. Mao, B. Liu, S. Zhang, Matrine alleviates staphylococcus aureus-induced acute lung injury in mice by inhibiting MLKL and NLRP3-mediated inflammatory activity, Eur. J. Pharmacol. 993 (2025) 177385, https://doi.org/10.1016/j.ejphar.2025.177385.
[18] N. Sun, H. Zhang, P. Sun, A. Khan, J. Guo, X. Zheng, Y. Sun, K. Fan, W. Yin, H. Li, Matrine exhibits antiviral activity in a PRRSV/PCV2 co-infected mouse model, Phytomedicine 77 (2020) 153289, https://doi.org/10.1016/j.phymed.2020.153289.
[19] M. Xu, Z. Ye, J. Liu, S. Zhu, Y. Chen, J. Cai, Y. Chen, L. Wang, L. Zhang, Q. Ye, A novel delivery system for the combined use of natural ingredients: the preparation of berberine hydrochloride-matrine liposomes and preliminary exploration of their anti-tumor activity, Molecules 29 (2024), https://doi.org/10.3390/molecules29215210.
[20] J. Lin, D. Zhou, T.A. Steitz, Y.S. Polikanov, M.G. Gagnon, Ribosome-targeting antibiotics: Modes of action, mechanisms of resistance, and implications for drug design, Annu. Rev. Biochem. 87 (2018) 451–478, https://doi.org/10.1146/annurev-biochem-062917-011942.

[21] N. Abed, P. Couvreur, Nanocarriers for antibiotics: a promising solution to treat intracellular bacterial infections, Int. J. Antimicrob. Agents 43 (2014) 485–496, https://doi.org/10.1016/j.ijantimicag.2014.02.009.
[22] E. Briones, C.I. Colino, J.M. Lanao, Delivery systems to increase the selectivity of antibiotics in phagocytic cells, J. Contr. Release 125 (2008) 210–227, https://doi.org/10.1016/j.jconrel.2007.10.027.
[23] G. Wang, H. Guo, M. Wei, Y. Wang, Z. Jin, J. Zhou, J. He, Y. Li, A hybrid-targeting nanoparticle for penetrable delivery of temozolomide to enhance glioblastoma therapy, Nano Lett. 25 (2025) 7989–7997, https://doi.org/10.1021/acs.nanolett.5c01609.
[24] X. Xiu, H. Fu, R. Zhang, S. Ma, P. Guo, Z. Li, Y. Zhu, F. Ma, Novel antigen-presenting cell-targeted nanoparticles enhance split vaccine immunity through microneedles inoculation, Int. J. Nanomed. 20 (2025) 5529–5549, https://doi.org/10.2147/IJN.S502724.
[25] R. Fukuda, Y. Fujiwara, H. Maeda, C. Pan, Y. Minayoshi, H. Yano, Y. Mizuta, M. Takano, R. Yamada, Y. Saito, K. Hirata, et al., Lymph node macrophage-targeted interferon alpha boosts anticancer immune responses by regulating CD169-positive phenotype of macrophages, Mol. Cancer 24 (2025) 132, https://doi.org/10.1186/s12943-025-02324-8.
[26] M. Chen, X. Liu, L. Kong, Y. Yu, J. Zang, X. Li, R. Guo, L. Zhang, Y. Liu, Efficacy assessment of glycyrrhetinic acid-modified liposomes loaded with doxorubicin hydrochloride and cucurbitine B for synergistic treatment of hepatocellular carcinoma, Int. J. Pharm. 673 (2025) 125360, https://doi.org/10.1016/j.ijpharm.2025.125360.
[27] L. Han, H. Zhan, X. Sun, Z.R. Zhang, L. Deng, A density-changing centrifugation method for efficient separation of free drugs from drug-loaded particulate delivery systems, AAPS J. 21 (2019) 33, https://doi.org/10.1208/s12248-019-0306-1.
[28] S.A. Peyman, J.R. McLaughlan, R.H. Abou-Saleh, G. Marston, B.R. Johnson, S. Freear, P.L. Coletta, A.F. Markham, S.D. Evans, On-chip preparation of nanoscale contrast agents towards high-resolution ultrasound imaging, Lab Chip 16 (2016) 679–687, https://doi.org/10.1039/c5lc01394a.
[29] H. Li, Y. Yin, C. Yang, M. Chen, F. Wang, C. Ma, H. Li, Y. Kong, F. Ji, J. Hu, Active interfacial dynamic transport of fluid in a network of fibrous connective tissues throughout the whole body, Cell Prolif. 53 (2020) e12760, https://doi.org/10.1111/cpr.12760.
[30] D.F. Alves, M.O. Pereira, S.P. Lopes, Co-immobilization of ciprofloxacin and chlorhexidine as a broad-spectrum antimicrobial dual-drug coating for poly(vinyl chloride) (PVC)-based endotracheal tubes, ACS Appl. Mater. Interfaces 16 (2024) 16861–16879, https://doi.org/10.1021/acsami.4c01334.
[31] P. Wu, P. Wang, W. Cao, N. Liu, H. Zou, G. Yang, Ultrafast and highly efficient laser extraction of matrine and oxymatrine from Sophora flavescens for the anticancer activity, ACS Omega 9 (2024) 38846–38854, https://doi.org/10.1021/acsomega.4c05003.
[32] F. Salehian, H. Nadri, L. Jalili-Baleh, L. Youseftabar-Miri, S.N. Abbas Bukhari, A. Foroumadi, T. Tuylu Kucukkilinc, M. Sharifzadeh, M. Khoobi, A review: biologically active 3,4-heterocycle-fused coumarins, Eur. J. Med. Chem. 212 (2021) 113034, https://doi.org/10.1016/j.ejmech.2020.113034.
[33] P. Stiefel, S. Schmidt-Emrich, K. Maniura-Weber, Q. Ren, Critical aspects of using bacterial cell viability assays with the fluorophores SYTO9 and propidium iodide, BMC Microbiol. 15 (2015) 36, https://doi.org/10.1186/s12866-015-0376-x.
[34] H. Shi, Q. Zhuang, A. Zheng, P. Zhan, Y. Guan, D. Wei, X. Xu, T. Wu, Antibacterial mechanism of N-PMI and the characteristics of PMMA-Co-N-PMI copolymer, Chem. Biodivers. 19 (2022) e202100753, https://doi.org/10.1002/cbdv.202100753.
[35] H. Ren, Q. Guo, B. Lin, Y. Liu, X. Wang, K. Huang, K. Wu, Biological applications on a novel composite hydrogel containing mesoporous silica nanoparticles loaded with insulin-like growth Factor-1 and vancomycin, J. Mater. Sci. Mater. Med. 36 (2025) 35, https://doi.org/10.1007/s10856-025-06884-5.
[36] S. Hanstein, T. Grochow, M. Motzing, S.A. Fietz, R. Hoffmann, C.G. Baums, S. Kahl, Comparative evaluation of antimicrobial peptides: effect on formation, metabolic activity and viability of Klebsiella pneumoniae biofilms, Front. Microbiol. 16 (2025) 1548362, https://doi.org/10.3389/fmicb.2025.1548362.
[37] L. Wu, Z. Du, L. Li, L. Qiao, S. Zhang, X. Yin, X. Chang, C. Li, Z. Hua, Camouflaging attenuated salmonella by cryo-shocked macrophages for tumor-targeted therapy, Signal Transduct. Targeted Ther. 9 (2024) 14, https://doi.org/10.1038/s41392-023-01703-1.
[38] R. Roy, M. Tiwari, G. Donelli, V. Tiwari, Strategies for combating bacterial biofilms: a focus on anti-biofilm agents and their mechanisms of action, Virulence 9 (2018) 522–554, https://doi.org/10.1080/21505594.2017.1313372.
[39] C. de la Fuente-Nunez, F. Reffuveille, L. Fernandez, R.E. Hancock, Bacterial biofilm development as a multicellular adaptation: antibiotic resistance and new therapeutic strategies, Curr. Opin. Microbiol. 16 (2013) 580–589, https://doi.org/10.1016/j.mib.2013.06.013.
[40] K. Golberg, K. Elouarzaki, B.E. Kagan, M. Shagan, N. Shemesh, E. Kramarsky-Winter, A. Ben-Zvi, Y.M. Nebenzahl, R.S. Marks, A. Kushmaro, Bio-informed synthesis of marine-sourced indole derivatives: suppressing gram-negative bacteria biofilm and virulence, BMC Biol. 23 (2025) 134, https://doi.org/10.1186/s12915-025-02234-7.
[41] J.W. Baek, S. Lim, N. Park, B. Song, N. Kirtipal, J. Nielsen, A. Mardinoglu, S. Shoaie, J.I. Kim, J.W. Son, A. Koh, et al., Extensively acquired antimicrobial-resistant bacteria restructure the individual microbial community in post-antibiotic conditions, npj Biofilms Microbiomes 11 (2025) 78, https://doi.org/10.1038/s41522-025-00705-x.
[42] S. Mukherjee, B.L. Bassler, Bacterial quorum sensing in complex and dynamically changing environments, Nat. Rev. Microbiol. 17 (2019) 371–382, https://doi.org/10.1038/s41579-019-0186-5.
[43] S. Azimi, A.D. Klementiev, M. Whiteley, S.P. Diggle, Bacterial quorum sensing during infection, Annu. Rev. Microbiol. 74 (2020) 201–219, https://doi.org/10.1146/annurev-micro-032020-093845.
[44] F.P. Vilela, C.G. Francisco, G.T.P. Brancini, D.D.P. Rodrigues, M.I.C. Medeiros, G.U. L. Braga, J.P. Falcao, Efficacy of photodynamic treatment with new methylene blue on planktonic cells and biofilms of salmonella isolated from vegetal sources in Brazil, Food Res. Int. 211 (2025) 116472, https://doi.org/10.1016/j.foodres.2025.116472.
[45] A. Wang, K. Yue, W. Zhong, G. Zhang, X. Zhang, L. Wang, Targeted delivery of rapamycin and inhibition of platelet adhesion with multifunctional peptide nanoparticles for atherosclerosis treatment, J. Contr. Release 376 (2024) 753–765, https://doi.org/10.1016/j.jconrel.2024.10.051.
[46] X. Chen, M. Sun, X. Ma, Y. Ma, B. Chen, Silencing hepatic PCSK9 via novel chimeric AAV8 mitigates the progression of atherosclerosis by inhibiting inflammation in ApoE(-/-) mice, Mol. Ther. Methods Clin. Dev. 33 (2025) 101390, https://doi.org/10.1016/j.omtm.2024.101390.